Title
Lensfree Computational Microscopy Tools and their Biomedical Applications

Author
Sencan, Ikbal

Publication Date
2013

Peer reviewed|Thesis/dissertation

UNIVERSITY OF CALIFORNIA

Los Angeles

Lensfree Computational Microscopy Tools and their Biomedical Applications

A dissertation submitted in partial satisfaction of the
requirements for the degree Doctor of Philosophy
in Electrical Engineering

by

Ikbal Sencan

2013

ABSTRACT OF THE DISSERTATION

Lensfree Computational Microscopy Tools and their Biomedical Applications

by

Ikbal Sencan

Doctor of Philosophy in Electrical Engineering

University of California, Los Angeles, 2013

Professor Aydogan Ozcan, Chair

Conventional microscopy has been a revolutionary tool for biomedical applications since its invention several centuries ago. Ability to non-destructively observe very fine details of biological objects in real time enabled to answer many important questions about their structures and functions. Unfortunately, most of these advance microscopes are complex, bulky, expensive, and/or hard to operate, so they could not reach beyond the walls of well-equipped laboratories. Recent improvements in optoelectronic components and computational methods allow creating imaging systems that better fulfill the specific needs of clinics or research related biomedical applications. In this respect, lensfree computational microscopy aims to replace bulky and expensive optical components with compact and cost-effective alternatives through the use of computation, which can be particularly useful for lab-on-a-chip platforms as well as imaging applications in low-resource settings. Several high-throughput on-chip platforms are built with this approach for applications including, but not limited to, cytometry, micro-array imaging, rare cell analysis, telemedicine, and water quality screening.[1]–[6]

The lack of optical complexity in these lensfree on-chip imaging platforms is compensated by using computational techniques. These computational methods are utilized for various purposes in coherent, incoherent and fluorescent on-chip imaging platforms e.g. improving the spatial resolution, to undo the light diffraction without using lenses, localization of

objects in a large volume and retrieval of the phase or the color/spectral content of the objects.[3], [5] For instance, pixel super resolution approaches based on source shifting are used in lensfree imaging platforms to prevent under sampling, Bayer pattern, and aliasing artifacts. Another method, iterative phase retrieval, is utilized to compensate the lack of lenses by undoing the diffraction and removing the twin image noise of in-line holograms. This technique enables recovering the complex optical field from its intensity measurement(s) by using additional constraints in iterations, such as spatial boundaries and other known properties of objects. Another computational tool employed in lensfree imaging is compressive sensing (or decoding), which is a novel method taking advantage of the fact that natural signals/objects are mostly sparse or compressible in known bases.[7] This inherent property of objects enables better signal recovery when the number of measurement is low, even below the Nyquist rate[8], and increases the additive noise immunity of the system.

The dissertation of Ikbal Sencan is approved.

Yahya Rahmat-Samii

Pei-Yu Chiou

Oscar M. Stafsudd

Aydogan Ozcan, Committee Chair

University of California, Los Angeles

2013

To the Light and to those who enlighten…

Table of Contents

Table of Figures

Acknowledgements

I would like to express my deepest gratitude to my advisor, Professor Aydogan Ozcan. He patiently spent hours discussing, advising and criticizing about my research with great care and gave me valuable feedback from the early stages of my graduate study to the final stages of completing this dissertation. He has always been incredibly accessible and excited about the projects. His commitment to excellence in research and communication skills has always inspired me. He will always remain a role model for me in the academia. I am very thankful to my committee members Professor Oscar Stafsudd, Professor Yahya Rahmat-Samii and Professor Eric Pei-Yu Chiou for their valuable contribution and support.

My dissertation research would have been impossible without the generous funding opportunities at UCLA Biophotonics Laboratory throughout my graduate studies and the support of Turkish Ministry of Education during my first year in UCLA.

My mentors, friends, and colleagues have collaborated with me in and enriched my journey in many different ways. I am very grateful to all current and past members of Ozcan Research Group, especially to Dr. Bahar Khademhosseinieh, Dr. Ting-Wei Su, Dr. Ertan Salik, Dr. Serhan Isikman, Dr. Onur Mudanyali, Dr. Hongying Zhu, Derek K. Tseng, Dr. Zoltan Gorocs, Dr. Ahmet Faruk Coskun, Alon Grinbaum, Wei Luo, Dr. Euan McLeod, Dr. Qingshan Wei, Steve Feng, Dr. Sungkyu Seo, Uzair Sikora, Justin Wong, Dr. Gabriel Biener, Stoyan Dimitrov, Dr. Waheb Bishara, Cetin Oztoprak, Anthony Erlinger, Oguzhan Yaglidere, Dr. Sam Mavandadi, Dr. Myungjun Lee, Dr. Serap Arpali, Dr. Caglar Arpali, Dr. Isa Navruz, Hamed Nilchi, Michael Mazon, Selen Alper, and Andrew Shih for their intellectual input, support and friendship. I am indebted to the Gulten and Nurettin Gunduz, Dr. Zeynep Sahin-Mencutek, Serife Ozger-Atar, Sumeyye Kocaman, Aysin Koca, Dr. Ozlem Demir and many dear friends that I could not list here, for their warm welcome and support during this great, yet challenging period. I also thank to Sukran Korkmaz and Berin Coban for helping me formatting the manuscript. Deeona, Mandy,

Michelle, Kimberly, Mildri, Rachelle, and Lori deserve special thanks for their continuous and kind help during my graduate study.

Finally, I would like to sincerely thank my family, my beloved parents, my grandmother, my sister Ilknur, my brother Ilker, and my lovely nephews Erkan and Orhan for their infinite love and invaluable support, for always being there for me throughout many years.

Vita

2012-2013	Teaching Assistant in Electrical Engineering University of California, Los Angeles, CA, U.S. EE101 - Engineering Electromagnetics and EE176 - Lasers in Biomedical Applications
2009-2013	Graduate Student Researcher at Ozcan Research Group University of California, Los Angeles, CA, U.S.
2008-2010	Master of Science in Electrical Engineering University of California, Los Angeles, CA, U.S.
2003-2007	Bachelor of Science in Electronics Engineering (Valedictorian) Fatih University, Istanbul, Turkey

Journal Publications and Book Chapters

Ikbal Sencan, Ahmet F. Coskun, Uzair Sikora, and Aydogan Ozcan, “Spectral Demultiplexing for Lensfree Holographic and Fluorescent On-chip Microscopy,” (2013) (To be submitted)

H. Zhu, I. Sencan, J. Wong, S. Dimitrov, D. Tseng, K. Nagashima, and A. Ozcan, ”Cost-effective and Rapid Blood Analysis on a Cell-phone,” Lab on a Chip (2013)

S.O. Isikman, W. Bishara, O. Mudanyali, I. Sencan, T. Su, D. Tseng, O. Yaglidere, U. sikora, A. Ozcan, “Lensfree On-Chip Microscopy and Tomography for Bio-Medical Applications,” IEEE Journal of Selected Topics in Quantum Electronics (2011) [Invited Manuscript]

Coskun, A. F., Su, T., Sencan, I., Ozcan, A. Lensless Fluorescent Microscopy on a Chip. J. Vis. Exp. (54), e3181, doi:10.3791/3181 (2011)

A.F. Coskun, I. Sencan, T. Su, and A. Ozcan, “Wide-field Lensless Fluorescent Microscopy Using a Tapered Fiber-optic Faceplate On a Chip,” Analyst (2011) [Joint first author]

A.F. Coskun, I. Sencan, T. Su, and A. Ozcan, “Lensfree Fluorescent On-Chip Imaging of Transgenic Caenorhabditis elegans Over an Ultra-Wide Field-of-View,” PLoS ONE (2011) [Joint first author]

B. Khademhosseini, G. Biener, I. Sencan, T. Su, A.F. Coskun and A. Ozcan, “Lensfree Sensing on a Micro-fluidic Chip using Plasmonic Nano-apertures,” Applied Physics Letters (2010)

B. Khademhosseini, G. Biener, I. Sencan, and A. Ozcan, “Lensfree Color Imaging On a Nano-structured Chip using Compressive Decoding,” Applied Physics Letters, 2010

A.F. Coskun, I. Sencan, T. Su, and A. Ozcan, “Lensfree Fluorescent On-Chip Imaging Over an Ultra-Wide Field-of-View using Compressive Sampling,” Special Issue of “Optics in 2010” Optics & Photonics News, December 2010

Ahmet F. Coskun, Ikbal Sencan, Ting-Wei Su, and Aydogan Ozcan, “Lensfree wide-field fluorescent imaging on a chip using compressive decoding of sparse objects,” Optics Express Vol. 18, Issue 10, pp. 10510-10523 (2010) [Joint first author]

Sungkyu Seo, Serhan O. Isikman, Ikbal Sencan, Onur Mudanyali, Ting-Wei Su, Waheb Bishara, Anthony Erlinger and Aydogan Ozcan, “High-throughput Lensfree Blood Analysis On a Chip,” Analytical Chemistry (2010)

Bahar Khadem-Hosseini, Ikbal Sencan, Gabrial Biener, Ting-Wei Su, Ahmet F. Coskun, Derek Tseng, and Aydogan Ozcan, “Lensfree On-chip Imaging using Nano-structured Surfaces,” Applied Physics Letters 96, 171106 (2010)

Derek Tseng, Onur Mudanyali, Cetin Oztoprak, Serhan O. Isikman, Ikbal Sencan, Oguzhan Yaglidere, and Aydogan Ozcan, “Lensfree Microscopy on a Cell-phone” Lab Chip (2010) – [Cover Article]

Onur Mudanyali, Derek Tseng, Chulwoo Oh, Serhan O. Isikman, Ikbal Sencan, Waheb Bishara, Cetin Oztoprak, Sungkyu Seo, Bahar Khademhosseini, and Aydogan Ozcan, “Compact, Light-weight and Cost-effective Microscope based on Lensless Incoherent Holography for Telemedicine Applications” Lab Chip (2010)

S. O. Isikman, I. Sencan, O. Mudanyali, W. Bishara, C. Oztoprak and Aydogan Ozcan, “Color and Monochrome Lensless On-chip Imaging of Caenorhabditis Elegans Over a Wide Field-of-View” Lab Chip (2010)

A. Ozcan, S.O. Isikman, O. Mudanyali, D. Tseng, I. Sencan, “Lensfree on-chip holography facilitates novel microscopy applications” SPIE Newsroom, (2010)

Ahmet F. Coskun, Ting-Wei Su, Ikbal Sencan, and Aydogan Ozcan, “Lensless Fluorescent Imaging On a Chip: A new Method Toward High-throughput Screening of Rare Cells,” Editors: Keith E. Herold & Avi Rasooly, Book Chapter in Biosensors and Molecular Technologies for Cancer Diagnostics, CRC Press (2012)

Chapter 1 Introduction

Conventional optical microscope has been a revolutionary tool for biomedical applications since its invention. Over the last decades, it has been significantly advanced to meet the high spatial and temporal resolution demands [9]–[12]. However; most of these advanced optical microscopy methods could not pass beyond the walls of high-end clinical and research settings due to their high cost and complexity. Computational microscopy, on the other hand, offers more accessible optical imaging platforms by replacing costly and complex optical hardware with computational software [6]. Lensfree on-chip imaging and sensing platforms are among the best examples of this practice.

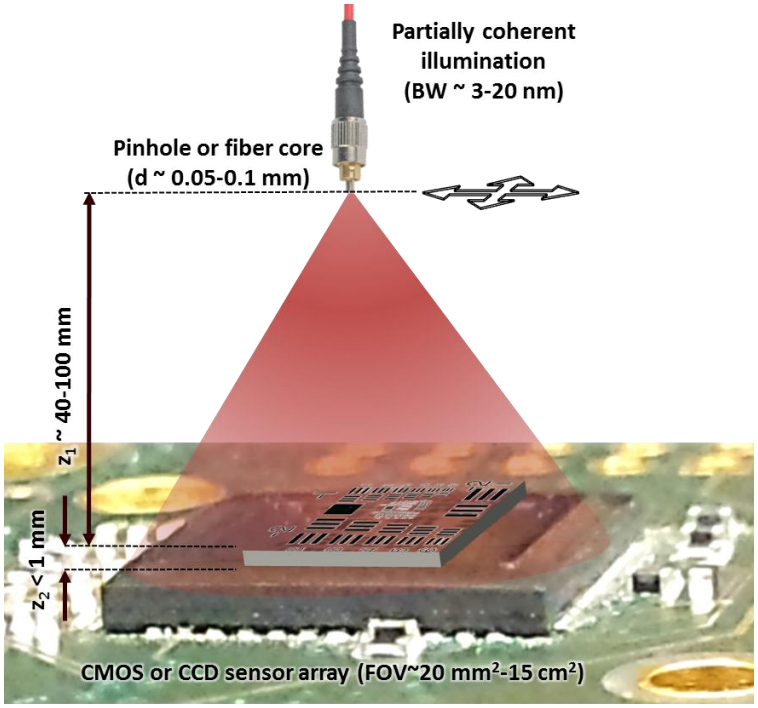

Figure 1: Partially coherent, on-chip holographic microscopy setup

Lensfree microscopy platforms also aims providing portability for field-use, compatibility with lab-on-a-chip devices and extremely wide field-of-view without sacrificing the resolution towards effectively addressing specific needs of applications like telemedicine, microfluidics and

high-throughput screenings.[1]–[5], [13]–[16] The lack of expensive optical components(e.g. lasers, high NA lenses), simplistic design, and effective use of widely available cameras and cellphones are the key factors of these platforms enabling these unique advantages. On the other hand, this approach also brings some challenges that needed to be computationally addressed not to trade-off the resolution.

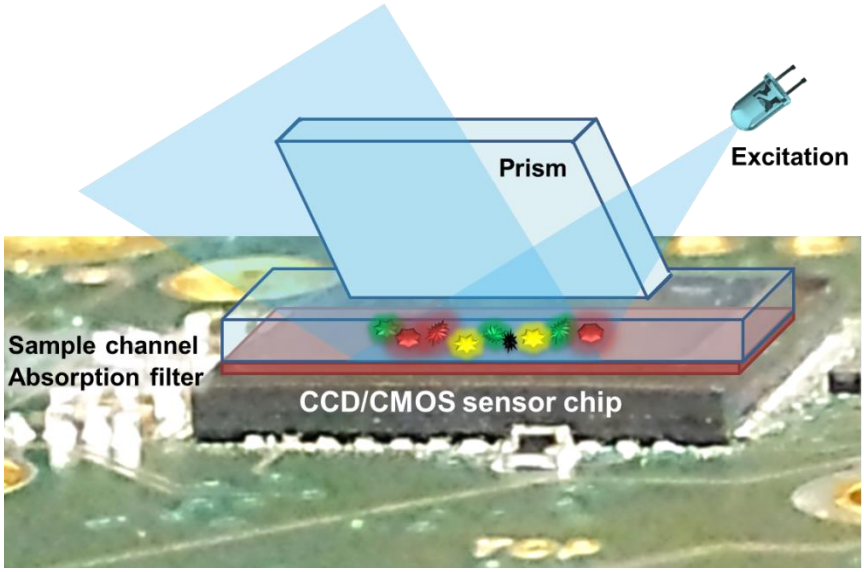

Figure 2: Fluorescent, Lensfree, Ultra-wide field-of-view, On-Chip, High-throughput Imaging Platform (FLUOCHIP)

The first immediate challenge is due to the absence of lenses: dealing with diffracted brightfield and fluorescent signatures, and twin image artifacts of inline-holograms. I employed iterative phase retrieval and compressive decoding algorithms to resolve these issues. Also, I further tailored them to provide computational solutions for insufficient temporal coherence of LEDs or sunlight and demultiplexing of simultaneous multicolor lensfree fluorescent signatures.

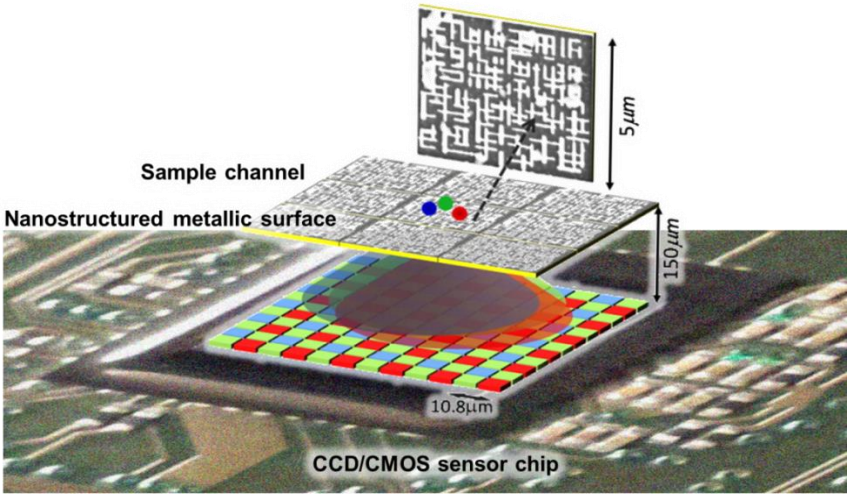

Figure 3: Microscopy with On-chip Nano-Apertures (MONA) Setup

The second challenge of performing on-chip microscopy is a result of placing the objects very close to the detector as demonstrated in Figures 1, 2 and 3. This short distance (<1mm) is necessary to maintain enough signal to noise (SNR) ratio and also allows all of the active area of the detector array to become the imaging field of view, which is uncoupled from the spatial resolution of the system. However, this also causes the pixel size of the detector to be a potential limiting factor towards achieving high spatial resolution. Although for most applications and biological objects of interest, this limitation is not significantly pronounced as demonstrated throughout Chapter 3.1 and 3.2; under-sampling and aliasing artifacts are observed for holographic imaging of objects like high resolution gratings as shown in Figure 4. These artifacts are well addressed by implementing pixel super resolution methods on lensfree geometries based on source [17] or object shifting [18]. I tailored and implemented this method for my holographic recoveries in Chapter 3.3 and 3.4.

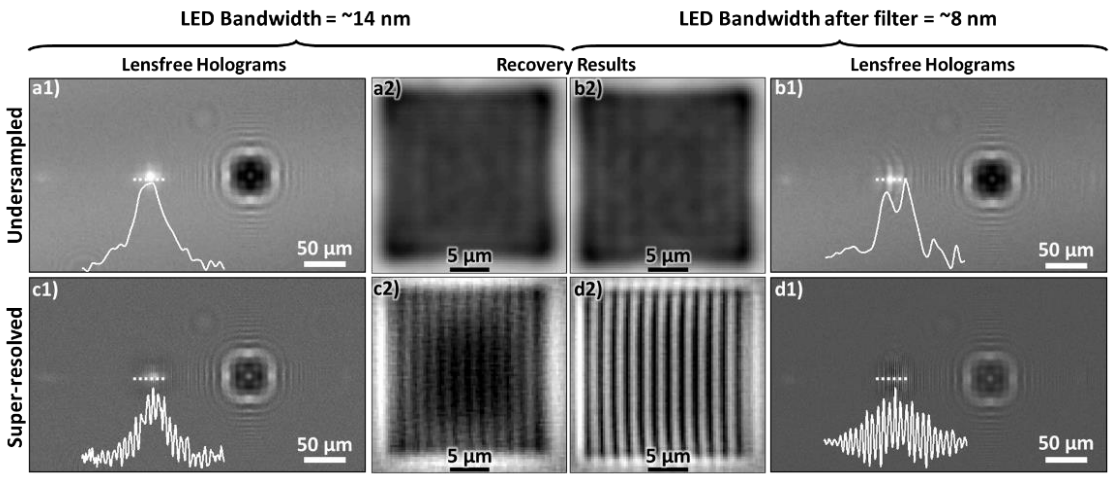

Figure 4: Effects of under-sampling and lack of temporal coherence for lensfree holographic on-chip microscopy. The use of pixel super resolution to overcome under-sampling issue

This dissertation is organized as follows: After providing a brief theoretical background on iterative phase retrieval, pixel super-resolution, and compressive sensing in Chapter 2, a set of lensfree computational microscopy tools, their applications are listed in two main categories in Chapter 3 and 4 based on the coherency levels of the imaging system. Finally, Chapter 5 provides a general conclusion on the reported lensfree computational microscopy tools and their biomedical applications.

Chapter 2 Methods

Computational on-chip microscopy provides compact, cost-effective, and robust imaging geometries for telemedicine and lab-on-a-chip applications, since it does not use any lenses or highly coherent light sources such as lasers. The lack of these components is successfully compensated using computational methods: Diffraction and twin-image artifacts are corrected by compressive decoding algorithms or iterative phase retrieval techniques whereas spatial under-sampling and aliasing problems are mitigated by pixel super resolution methods as mentioned in the introduction chapter.

This section will focus on the theoretical aspects of three methods that are mainly employed in lensfree computational microscopy platforms: Iterative Phase Retrieval, Pixel Super-Resolution, and Compressive Decoding.

2.1 Iterative Phase Retrieval

Iterative phase retrieval [19], [20] is a quite mature field vastly studied while several decades. There are various approaches to iteratively retrieve the lost phase information, from the recorded intensity pattern(s) by enforcing additional constraints [19]–[23] These constraints include but not limited to multiple intensity images recorded in different depths, assumptions about the optical nature of the object (e.g. phase or amplitude only objects), multiple intensity images recorded under different illumination conditions (e.g. wavelength, spatial distribution), known phase or amplitude modulations before the detection, and known field outside a rough object mask. I adapted an object support based phase retrieval approach for lensfree holographic imaging applications listed in this dissertation since the objects of interest were sparse.[3] The constraint applied here is that the objects have finite spatial confinement, and surrounding background is known. By enforcing this condition, this technique is capable of iteratively recovering the phase of the diffracted field incident on the detector from a single intensity measurement. As a result, the complex field (amplitude and phase) of the

lensfree holograms can be back-propagated and focused to the object plane, thereby allowing reconstruction of the objects free from twin-image contamination. This approach can be briefly explained as follows: First, the raw holograms are interpolated by a factor of four to six, using cubic spline interpolation. Though this interpolation step does not immediately enrich the information content of the holograms, it still helps towards achieving more accurate phase recovery and higher resolution in the reconstructed image. It helps to create a better object support mask by smoothing the objects in the initial back-projection of the hologram. It also introduces higher spatial frequencies in the hologram, which initially do not carry energy. Then gradually, the frequency content is extrapolated to these higher spatial frequencies as iterative phase reconstruction steps detailed below are followed. Then the detected intensity is back-propagated to the object plane with the Rayleigh-Sommerfeld integral without any approximations (like paraxial or far-field) by using the angular spectrum method, assuming a field phase of zero as an initial guess [24]. Specifically, after taking the 2D Fourier Transform of the square root of the measured intensity it is multiplied with the optical transfer function that for propagation:

$$H(f_x, f_y) = \begin{cases} \exp\left(j2\pi z \left(\frac{n}{\lambda}\right)\sqrt{1 - \left(\frac{\lambda f_x}{n}\right)^2 - \left(\frac{\lambda f_y}{n}\right)^2}\right) & , \sqrt{f_x^2 + f_y^2} < \frac{n}{\lambda} \\ 0 & , \text{otherwise} \end{cases} \quad (1)$$

, where z is the forward propagation distance; λ is the illumination wavelength; f_x and f_y are the spatial frequencies along the x- and y-directions, respectively; and n is the refractive index of the propagation medium.

Since the on-chip platforms introduced in Figure 1 detect partially coherent inline holograms, this back-projection of recorded intensity serves as a great initial estimation of the object field to feed the phase retrieval algorithm; although the recorded image is not necessarily treated as a hologram. The object support mask is simply created at this first backprojection. Depending on how complicated the objects are, the mask is defined either by global or local

thresholding the intensity of the field at the object plane or by locating its regional maxima and/or minima. Then it is iterated back and forth between the object and detection planes by enforcing the constraints at each level. The individual cell is treated to be illuminated with a coherent light and due to their microscopic cross-sections, and the incident wave on each cell is assumed to be a plane wave. On the object plane ($z=z_o$), I enforce the background outside the finite object support (S) while preserving the field inside the support. This background (B) can either be the back-projected intensity image of the same field of view captured before loading the object or simply the mean value of the field at the object plane as a flat background. The updated field in i^{th} iteration on the object plane can be written as follows, where the superscripts denote the iteration step and the subscripts denote the distance z from the detector.

$$U_{z_o}^{(i+1)}(x,y) = \begin{cases} m^{(i)} \cdot B_{z_o}(x,y), & (x,y) \notin S \\ U_{z_o}^{(i)}(x,y), & (x,y) \in S \end{cases} \quad (2)$$

$$m^{(i)} = \text{mean}\left(U_{z_o}^{(i)}(x,y)\right) / \text{mean}\left(B_{z_o}(x,y)\right) \quad (3)$$

On the detector plane (z=0), I enforced the square root of the measured intensity image in each iteration while keeping the phase.

$$U_0^{(i+1)}(x,y) = \left|U_0^{(0)}(x,y)\right| \cdot \exp\left(j \cdot \text{angle}\left(U_0^{i}(x,y)\right)\right) \quad (4)$$

Using this spatial-mask-based greedy phase retrieval method on partially coherent on-chip holograms; recovery results converge with only 5-10 iterations without stagnations or local minima problems [cite] to a complex object field cleaned from twin image artifacts. Because I preferred to use the angular spectrum method for propagations between planes by employing multiple Fast Fourier Transforms (FFT), the recoveries are also quite fast, in terms of computation time. This image reconstruction time can be as low as <1 s, up to an image size of ~20 megapixels using a graphics processing unit (GPU) (CUDA-enabled NVIDIA GeForce GTX 285).

Using such a phase retrieval algorithm instead of a regular holographic reconstruction method has certain advantages. For large and highly scattering objects, the scattered light cannot always effectively interfere with the reference, so that self-interference terms become no longer negligible, which is very commonly assumed to be negligible in holographic reconstructions. However, unlike the holographic reconstruction methods, the phase recovery approach treats the detected quantity as the intensity of the complex field and tries to iteratively recover its phase. Therefore, the phase-recovery-based reconstruction approach is especially useful for lensfree imaging of highly scattering cells or larger-scale organisms where the self-interference terms start to dominate over holographic terms.

2.2 Pixel Super-Resolution

When the lensfree holograms of the objects contain very high frequency fringes that cannot be well sampled with the physical pixel size, undersampling and aliasing artifacts are observed in the lensfree holograms and this reflects as resolution loss to the microscopic recoveries as demonstrated in Figure 4. To address this problem, a de-aliasing approach called “pixel super resolution” is adapted to lensfree holographic imaging geometry. Pixel super resolution is widely used in real life, for security applications since infrared cameras are quite low-resolution compared to the imaging standards in visible range. It is important to clarify that this approach is different than the famous super-resolution methods like STED, PALM, or SIM [9]–[11], [25] which does aim to beat the diffraction limit. The main idea behind ‘pixel-super resolution’; however, is to beat the undersampling and aliasing limitations and it is practiced by capturing multiple slightly shifted low resolution frames from a scene and fusing them in a way that they will form a well-sampled, high-resolution image of the same filed-of-view. These low resolution frames with relative translational sub-pixel shifts are mostly captured either by moving the detector or the objects. Due to the unique geometry of lensfree, on-chip, holographic imaging platforms, these subpixel shifts are very practically achieved by moving the light

sources, as well. [17] As a result of the z_1 and z_2 ratio in Figure 1, a millimeter range shift in source level is projected as micrometer level object signature shifts on the detector level.

In this dissertation, I employed pixel super resolution on RGB (Red, Green, Blue) lensfree on-chip holograms of objects illuminated with broadband light sources. I used a modified version of the algorithms reported in [6], and [17], which can be summarized as follows: Since my holograms are recorded with a color sensor and illuminated with broadband light sources, all red, green and blue channels of my lensfree images contained information. First, RGB pixels are separated and low resolution frames (L) are grouped based on which color channels that they are read. Then a small region that contains a reference circular object is selected from the wide field of view to estimate the relative shifts of all Ls with respect to the first frame. These shifts are estimated by running cross-correlating between these selected regions for a color channel (for instance green) and then locating the peaks in these correlation maps. After the shifts for each color channels are calculated based on these estimated shifts, a high resolution frame (H) is reconstructed per color channel by minimizing the following cost function (regularized maximum likelihood estimation), where k represents the shift number, L_k is the measured low resolution image, H_{hpf} is the high-pass filtered high resolution image, and α is the regularization parameter.

$$\mathrm{f(H)} = \left(\frac{1}{2}\right) \left\| \mathrm{L}_k - \tilde{\mathrm{L}}_k \right\|_2^2 + \left(\frac{\alpha}{2}\right) \left(H_{hpf}^t H_{hpf}\right) \qquad (5)$$

$$Calculated\ Low\ Resolution\ Image, \qquad \tilde{\mathrm{L}}_k = \sum W_k H$$

2.3 Compressive Sensing

Digital revolution in sensing provided us the ability to collect massive amounts of data from various types of sensors, spanning the electromagnetic spectrum e.g. visible, acoustic, infrared, radio frequency ranges. This ability also brings an increasing pressure on sensors, hardware, and algorithms and requires finding efficient ways of acquiring, storing and

processing this deluge of data.

Transform coding [26] is one of the most widely used approaches to handle this problem. In this approach, a signal (e.g. N-pixel image x) is first completely acquired. Then its set of coefficients are computed for a chosen domain such as Fourier, wavelet etc. After locating the most significant K coefficients, the transform coder discards all the value and location information except ones belong to these K chosen elements. So transform coding can be shortly described as “Sample first, question later” type of approach which is very inefficient when N>>K. For a long time, it has been tried to directly estimate the set of large coefficients that will not be discarded by the transform coder. During the last decade, compressive sensing made significant progress towards achieving this goal as a very clever way of acquiring the compressed data by replacing the regular sampling with more general measurements. Compressive sensing can be described as a “Sample less, compute later” type of approach, unlike transform coding.

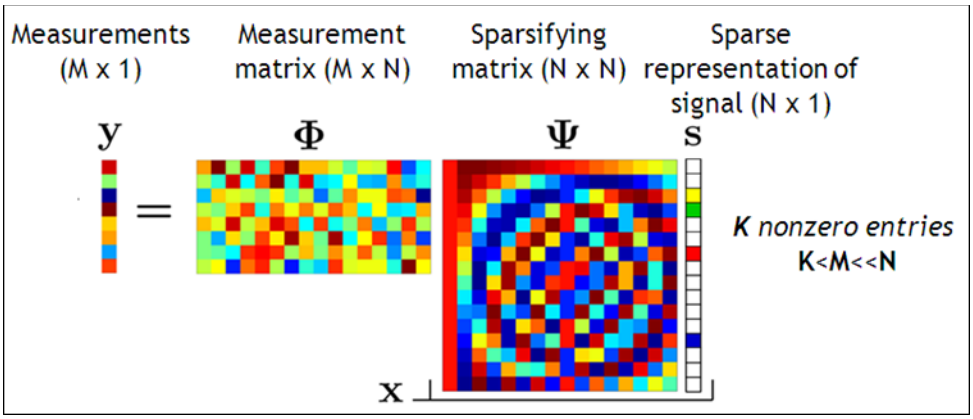

Figure 5: Elements of Compressive Sensing [8]

Compressive sensing theory [27], [7] relies on the fact that most of the natural or manmade signals are sparse or at least compressible in a transformation domain. The sorted transform coefficients of a “sparse” signal contain only a few (K<<N) nonzero components whereas these coefficients from a “compressible” signal show an exponentially decaying characteristic. For instance, while smooth images are usually sparse in Fourier domain, images

with sharp corners and edges are sparse in wavelet domain. There are also many examples where the object itself is already sparse in spatial domain like distribution of fluorescently labeled cells or particles, which will be shown later in this prospectus.

Once assuring the signal can be represented sparsely in a certain basis, the measurement matrix should be chosen whose rows represent M (M = O(Klog(N/K))<<N) number of individual linear measurements. The measurement matrix should be chosen such that it is incoherent with sparsifying matrix and they should satisfy the "Restricted Isometry Property (RIP) [28]". In other words, these two bases (measurement and sparsifying) together should form a linear orthogonal transform set in order to successfully recover the signal x from its reduced dimensional projection y. Although it is very hard to design/test arbitrary pairs of bases satisfying RIP, it is shown that a uniformly distributed random basis is incoherent with any fixed basis with high probability. This practically means that M random projections (K<M<<N) can be used to acquire data.

The last step is to recover the signal back from these linear measurements.

$$\mathrm{y} = \Phi\mathrm{x} = \Phi\Psi\mathrm{s}\ . \quad (6)$$

For this end, several algorithms are suggested like ℓ_p norm minimization, which can be defined as

$$\|x\|_p = \left(\sum_{i=1}^{N}|x_i|^p\right)^{1/p}. \quad (7)$$

Using the pure least square minimization (p=2) is not a preferable method for finding a sparse s' such that

$$\psi\mathrm{x}' = \psi\varphi\mathrm{s}' = \mathrm{y} \qquad (8)$$

since it is minimizing the energy and almost never provides sparse solutions. When p=0, the recovered value of sparse representation of the signal becomes the

$$\mathrm{s'} = \arg\min||\mathrm{s}||_0, \qquad (9)$$

which simply means to minimize the number of nonzero values. However this problem is very

complex to solve, as it requires checking all $\binom{N}{K}$ possible subspaces. At this point, recovery algorithms minimizing the ℓ_1 norm (Basis Pursuit) are ideal because they can easily minimize magnitude summation which also provides the sparsest solution with a high probability. As a result of great efforts for finding the optimum way of recovery, there are several powerful code packages available. In this work, ℓ_1 or total variation (TV) regularized least-square minimization algorithms are preferred (ℓ_1_ls [29] and TwIST[30]) both specially because of their performance, speed and, ease of use for large scale data.

$$\tilde{\mathrm{x}} = \mathrm{argmin}(\left\|\mathrm{Ax} - \mathrm{I}_{\mathrm{det}}\right\|_2^2 + \beta\psi(\mathrm{x})) \quad (10)$$

$$\text{Total Variation(TV)},\ \psi(\mathrm{x}) = \sum_{\mathrm{i}} \sqrt{\left(\Delta \mathrm{h}_{\mathrm{i}}\ \mathrm{x}\right)^2 + \left(\Delta \mathrm{v}_{\mathrm{i}}\ \mathrm{x}\right)^2} \quad (11)$$

$$\ell 1 \text{ Norm}, \qquad \psi(\mathrm{x}) = \|\mathrm{x}\|_1 = \sum_{i=1}^{N} |x_i| \quad (12)$$

Incoherent lensfree imaging applications are quite straightforward to approach with compressive sensing techniques because they are linear in intensity and fluorescent objects are mostly sparse in spatial domain. Thus, I widely employed compressive decoding approaches in different incoherent lensfree imaging platforms by tailoring the forward model –measurement matrix- as it will be mentioned later in this prospectus. It is also shown that CS can be applied to coherent imaging systems [31], [32], [33], which are nonlinear in intensity measurements. In Chapter 3.4, I also used it to demultiplex sunlight holograms into narrow spectral channels, which requires solving a deeply underdetermined problem.

In the following two chapters, I introduce some lensfree computational microscopy tools and their biomedical applications. I preferred to present them under two broad categories based on the coherence level of their imaging methods: Partially-Coherent Imaging and Sensing Applications and Incoherent Imaging Applications.

Chapter 3 Lensfree Partially-Coherent Imaging and Sensing Applications

The methods and applications reported in this chapter are already published as journal articles in the following references: [1]–[4], [34].

On-chip imaging of biological objects based on partially-coherent holography has a great potential to complement the conventional optical microscopy with its compact and high-throughput solutions. Along this line, the lensfree, inline holography with a compact geometry particularly is utilized in the computational microscopy tools presented in this manuscript. This geometry makes them mechanically robust and field-portable systems opt for applications like telemedicine. I will briefly explain the basics of this lensfree, partially-coherent, on-chip imaging platforms, before giving some examples of their applications.

3.1 High-throughput Holographic On-chip Imaging Platform

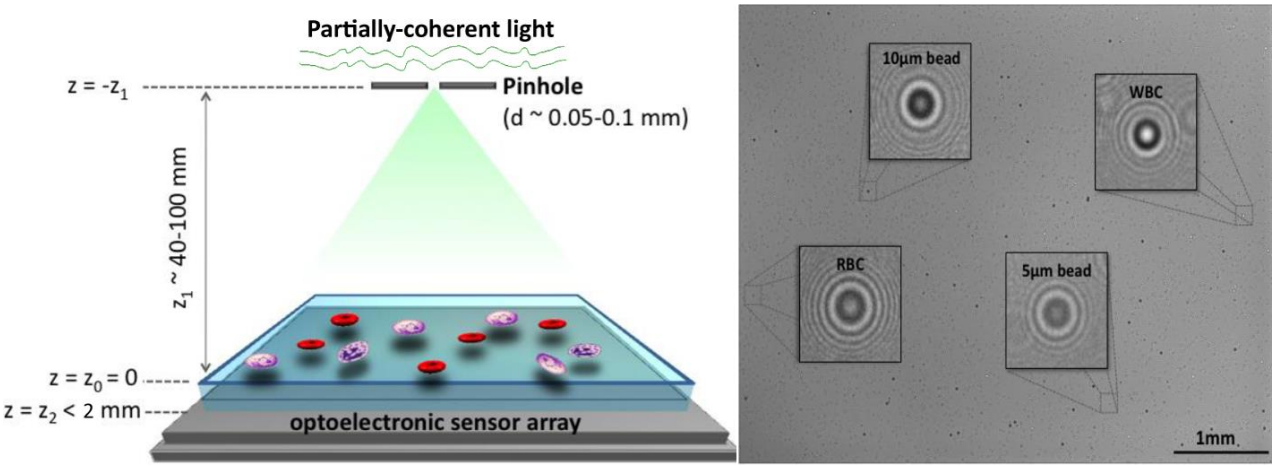

Figure 6: Schematic of the lensfree, on-chip, holographic imaging of different objects with unit fringe magnification over the whole sensor active area[4]

As illustrated in Figure 6, objects of interest are placed directly on the top of the optoelectronic sensor array (CCD or CMOS). So, the typical distance between the objects and the sensor active area (z_2) is below 2 mm. A partially-coherent light source e.g. LED, which is placed 40-100 mm above the objects (z_1) is first filtered with a large pinhole with a diameter of d=0.05-0.1mm before it uniformly illuminates the objects. While a small portion of the

illumination is scattered by the objects, s(x,y), the remaining form the unperturbed reference light r(x,y). So, the intensity to be detected by the optoelectronic sensor can be written as

$$I = |r(x, y, z_0) + s(x, y, z_0)|^2$$

$$= |s(x, y, z_0)|^2 + |r(x, y, z_0)|^2 + r(x, y, z_0) \cdot s^*(x, y, z_0) + s(x, y, z_0) \cdot r^*(x, y, z_0) \quad (13)$$

The pure scattered light intensity carrying the information about the fine details of the objects is usually too weak to detect and buried under the strong uniform reference light intensity. However interference of them within a coherence diameter that is typically larger than the signature of biological objects, allows the heterodyne detection of these details. To recover the complex field right after the object plane, I utilized a phase retrieval algorithm which iteratively improves the field estimation by forcing the rough guess of object boundaries and the intensity measurement as constraints. It is important to remind that these intensity measurements are also partially-coherent inline holograms, providing a very good initial estimation of the complex object field. This property allows the code to quickly converge without facing stagnation of local minima problems. Thus, the phase and amplitude images which are clean from twin-image artifacts are recovered, using only 5-20 iterations, within <1sec using a graphics processing unit (GPU).

The performance of these platforms for biomedical applications is first demonstrated on blood. Figure 7 shows the lensfree hologram of red blood cells (RBC) with sample concentrations of ∼102 000 cells/*μ*L and 394 000 cells/μl. Despite the severe overlap of the RBC signatures, the reconstruction matches well with the 10X microscope comparison. [3]

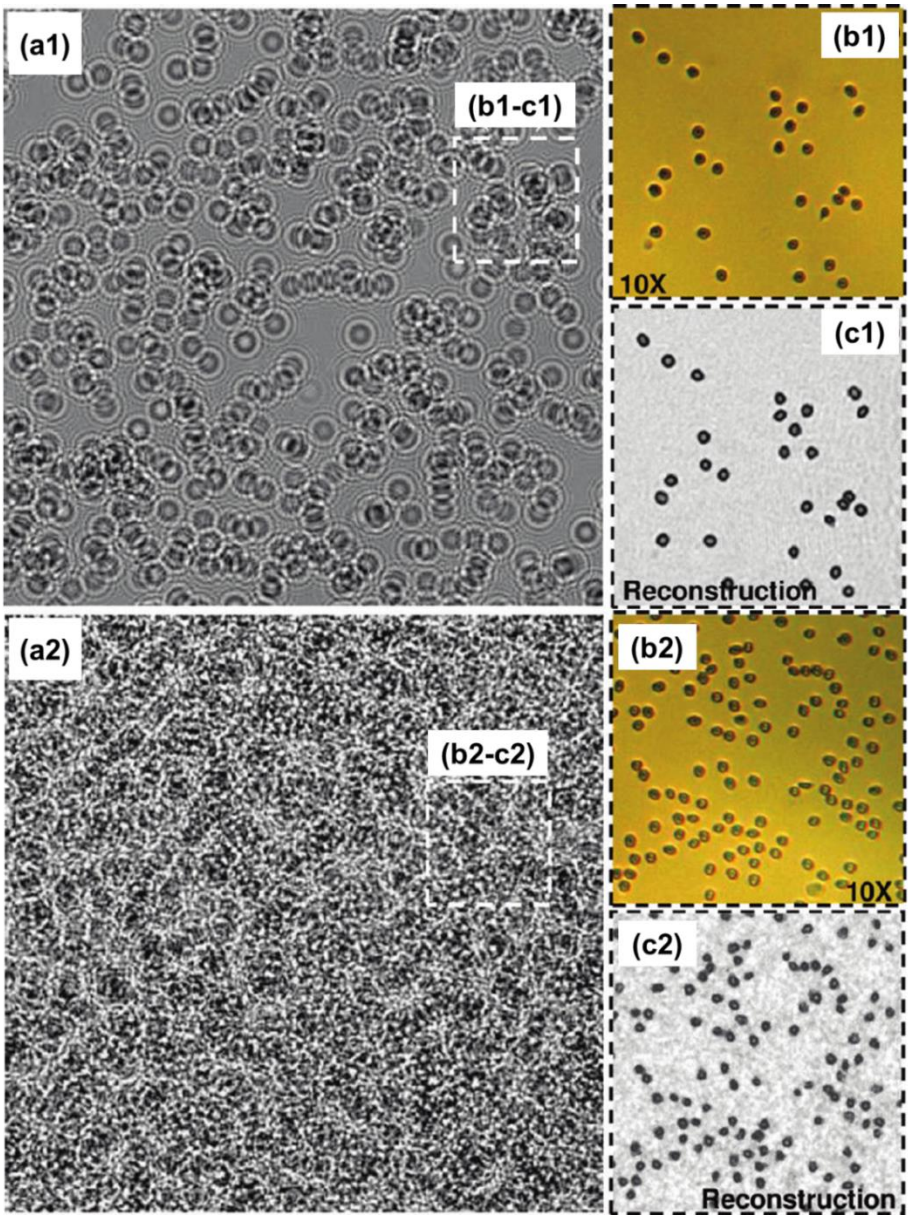

Figure 7: (a1 and a2). The lensfree holographic image of RBCs with density of 102 000 cells/μL and ~394 000 cells/µl., cropped from a much larger field of view of ~24 mm^2. Individual holographic signatures of the cells at such high cell densities severly overlap. (c1 and c2) Thje phase retrieval results and their microscope comparisons (10x objective) (b1 and b2) are well matching. [3]

Then these experiments are repeated with various concentration levels and counting and volume estimation results are compared against the manual microscope counts and coulter counter (Model Coulter LH750, Beckman Coulter) results. An automated RBC count up to 400000 cells/µl with <5% accuracy is reported with reconstructed images. Also the total cell

volume is quite accurately estimated (Figure 8, top inset) by using the unwrapped phase images of the cells [35] assuming that RBCs are phase only objects with refractive index of ~1.4. Also, automated white blood cell (WBC) count results are demonstrated using the lens-free holographic imaging platform shown in Figure 8 (bottom), as a function of the whole blood dilution factor (8×, 12×, and 16×, 24 samples per dilution factor). The average WBC density of this patient is estimated to be 4875, 4805, and 4251 WBCs/μL, respectively. These results show a nice agreement with the Coulter Counter result, 4700 WBCs/μL. [3]

Next, this geometry is used for demonstration of high-throughput, color imaging of C. elegans worms which are widely studied microscopic model organisms [1]. This platform is very suitable for such an application because of its integration with microfluidics is straightforward, and it can simultaneously image ~100 worms through its wide FOV (24 mm^2). Moreover, in this application, color of the objects is also demonstrated as shown in Figure 9 for the stained C. elegans sample. Color imaging is achieved by digitally combining recoveries of three RGB (wavelengths of 450, 550 and 650 nm) sequentially recorded holograms.[1]

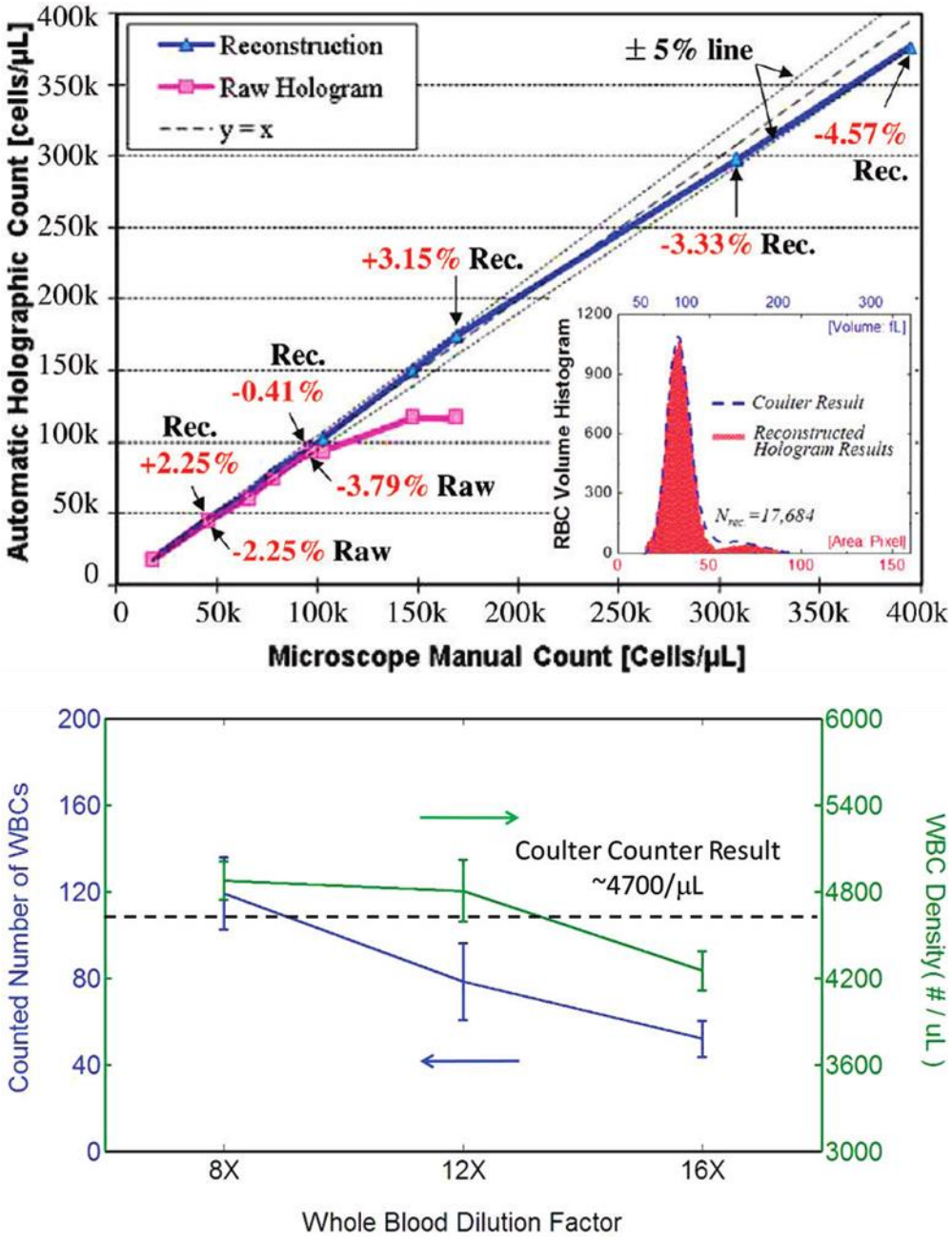

Figure 8: (Top) Automated holographic counting of RBCs in the hologram domain (pink curve) and the reconstructed image domain (blue curve) compared against manual microscope counts. The counting error of reconstructed signatures remains within 5% range up to 400k cells/µL (Top, inset) Shows calculated volume histogram of RBCs compared against a Coulter counter (Model Coulter LH750, Beckman Coulter), result. (Bottom) WBC counts and density estimation from a patient for 3 different whole blood dilution factors (8x, 12x, 16x). [3]

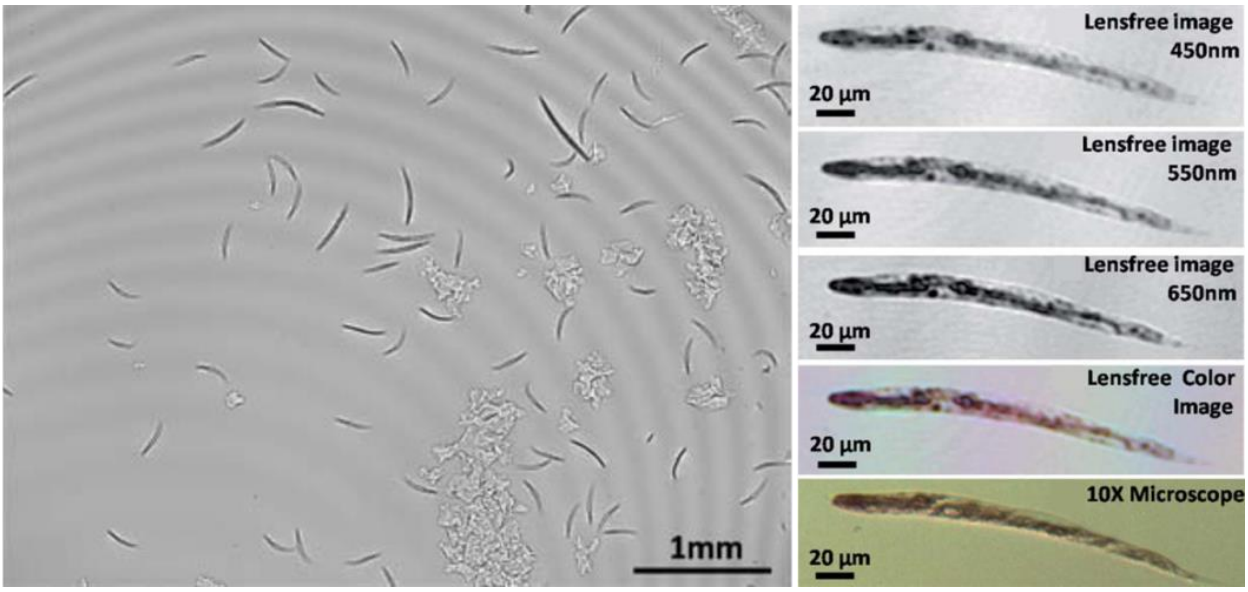

Figure 9: (left) A lensfree, partially-coherent hologram of C. Elegans worms that is captured with the platform shown in Figure 6. Digital processing of this raw hologram permits simultaneous on-chip imaging of C. Elegans samples over >24 mm^2 FOV. Using a state of the art GPU, this digital reconstruction process takes <1 s over the entire imaging FOV. (right) Digitally reconstructed holographic images of a C. Elegans sample stained using Ponceau S red, captured with illumination wavelengths at 450 nm, 550 nm and 650 nm, respectively (FWHM = 15 nm in each case). Lensfree color image obtained by fusing the reconstructions at each wavelength is compared against the brightfield microscope image obtained with a 10X objective-lens.[1]

3.2 Portable Holographic On-Chip Microscopes for Telemedicine Applications

After some initial bench-top applications for clinical and research settings, this computational microscopy approach is also used to develop a tool that better fulfills the imaging needs of resource-limited settings. For this end, a compact, light-weight and cost-effective telemedicine microscope is demonstrated.[2] This lensfree on-chip microscope is smaller than 4.2cm × 4.2cm × 5.8cm, weights ~46 grams, and achieves sub-cellular resolution over a large field of view of ~24 mm^2 as shown in Figure 10. Since this compact and light-weight microscope is based on digital in-line, partially-coherent holography, it does not need any lenses, bulky optical/mechanical components or coherent sources such as lasers. Instead, it utilizes a simple LED and a compact optoelectronic sensor-array to record lensfree holograms of the objects, which then permits rapid digital reconstruction of transmission objects. Furthermore, due to its

large pinhole size, this lensfree incoherent holographic microscope has orders-of-magnitude improved light collection efficiency and is very robust to mechanical misalignments; it may offer a cost-effective tool especially for telemedicine applications involving various global health problems in resource limited settings. Figure 10 shows the images of various blood cells recorded with this standalone platform and their reconstructions matching well to the 40x microscope comparisons. It is important to note that these entire objects are digitally cropped from the wide FOV of ~24 mm^2 in order to show the imaging performance.

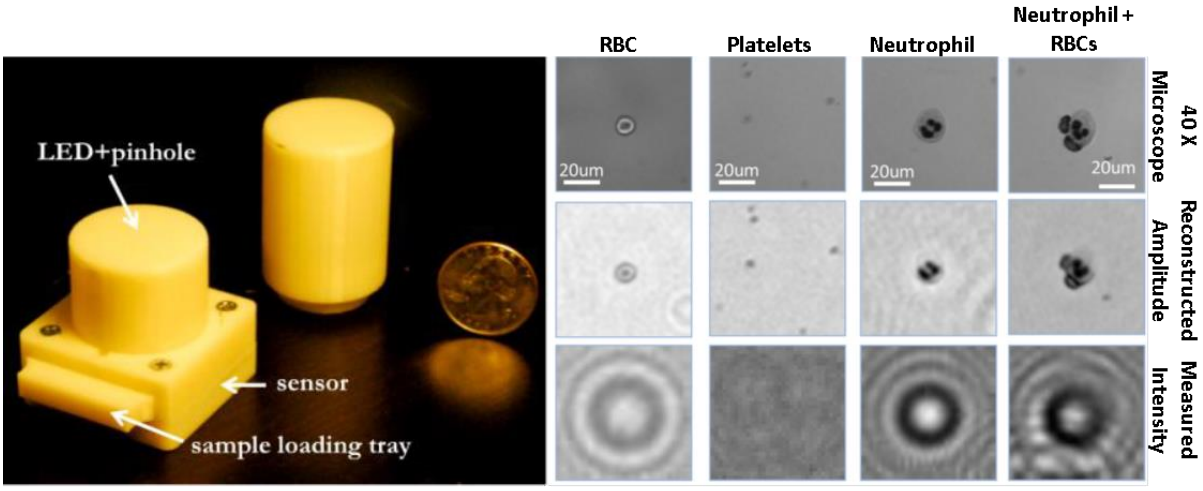

Figure 10: (Left) The lensfree telemedicine microscope utilizing an LED source (λ = 591 nm) with a photon-efficient (50–100 μm diameter) aperture of in front. The LED and the sensor are powered through USB connection from the side. The cylindrical structure is simply a hollow tube that the spatially filtered light propagates within before illuminating the objects. Light tubes of different lengths can be interchangeably used to achieve different degrees of spatial coherence depending on the requirements of the application. Objects are loaded onto the sensor-chip using the sample tray. (Right) Various objects imaged using the lensfree telemedicine microscope on the left are illustrated and compared against 40× objective-lens (NA=0.6) images of the same FOV. The bottom row shows the recorded intensities that are digitally processed to reconstruct the middle row images. [2]

This platform is further improved to several compact handheld microscopes like the high-resolution handheld microscope based on pixel super resolution [36] and the handheld tomography device [37] which will not be covered in this manuscript. Another dimension of this work which is going to be mentioned here is the lensfree cellphone microscope [13], where the on-chip, lensfree, partially-coherent holography method is used to turn a regular camera phone

into a microscope with a simple ~38 gram attachment as shown in Figure 11 (a) and (b). This attachment is very similar to the handheld unit except that this custom made plastic piece carrying a battery-powered LED source, is specially designed to fit to the cellphone like its back cover. It also utilizes the RGB sensor of the cellphone to record the raw format, Bayer patterned intensity images. Since an LED with 587 nm center wavelength is used for illumination, the blue channel is highly corrupted by noise. Therefore, preprocessing is needed before the rough boundary estimation and initial estimation of the object. The two high SNR channels (red and green) channels of the acquired raw holographic image are balanced using a background image. The missing blue pixels are estimated by using a demosaicing algorithm [38] not penalizing the edges in order to initially guess the object and automatically detect its rough boundaries. Then specially tailored iterative phase retrieval algorithm is used to enforce the object mask and the measured intensity at red and green channels as two constraints to converge the final microscopic image. The complete recovery process is summarized in Figure 11-c. Several experiments is conducted using this cellphone microscope on various biological samples like blood cells, platelets and waterborne parasites and compared its performance against regular microscope images as illustrated in Figure 11-d.

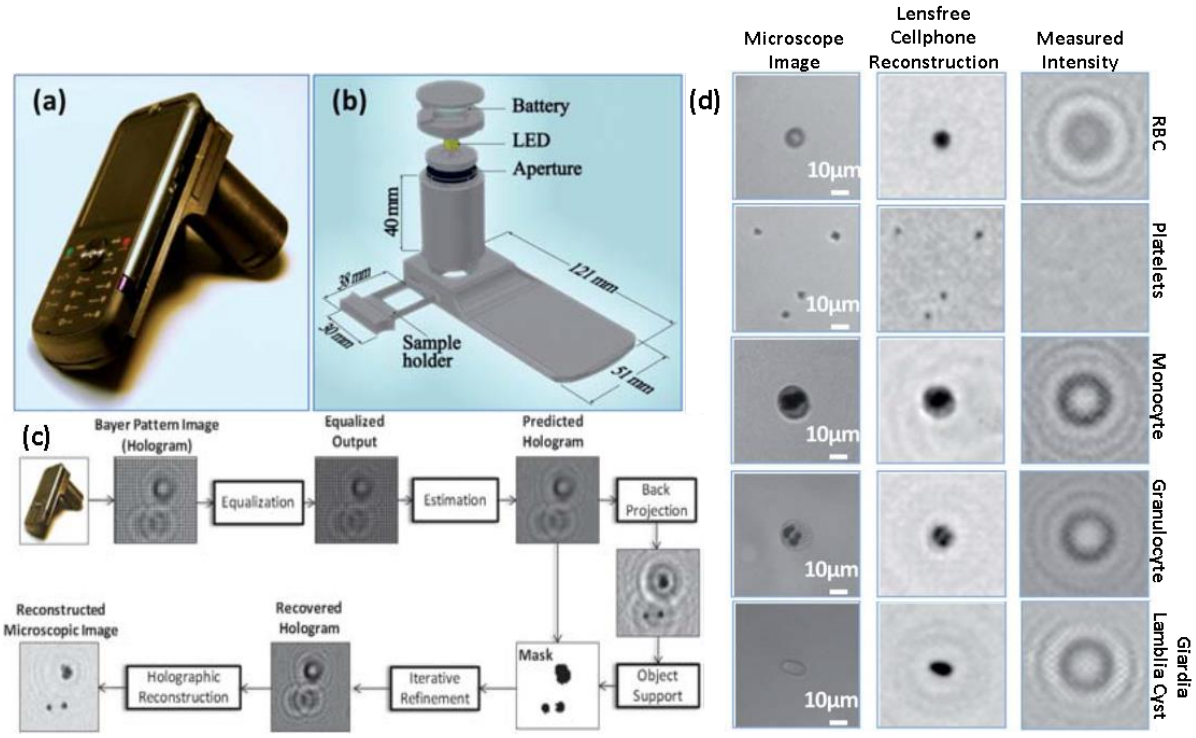

Figure 11: (a) The lensfree cellphone microscope which operates based on incoherent in-line holography is shown. The additional hardware installed on the cellphone weighs <38 grams (<1.4 ounces) and is composed of an inexpensive light emitting diode (at 587 nm) with an aperture of ~0.1mm butt-coupled to the LED. This cellphone microscope does not utilize any lenses or other bulky optical components and operates with a unit fringe magnification to claim the entire active area of the sensor as its imaging field of view. The samples to be imaged are loaded from the side through a mechanical sample holder. (b) Schematic diagram of the microscope attachment shown in (a) is illustrated. (c) De-Bayering algorithm developed to create monochrome holographic images from Bayer patterned, raw-RGB output of the lensfree cellphone microscope is summarized. Red and green channels of the acquired raw holographic image are equalized using a background image that was recorded with identical illumination conditions as the object. Blue pixels are estimated from their red and green neighbors using an edge-aware interpolation approach and are further refined through an iterative recovery process with the help of an automatically generated object support mask. Finally, the recovered hologram is up-sampled and fed into the object-support based phase retrieval algorithm to create the corresponding microscopic images of the objects. (d) Imaging performance of the lensfree cellphone microscope shown in (a) is compared against a regular microscope (10X objective lens, 0.25 numerical aperture) for red blood cells, white blood cells (monocytes and granulocytes), platelets, and Giardia lamblia cyst. The lensfree holograms captured by the cellphone sensor are digitally processed within less than 30 msec to reconstruct microscopic images of the specimen as shown on the middle column.[13]

3.3 Spectral Demultiplexing of On-chip Polychromatic Holograms

Computational microscopy platforms reported so far in this manuscript all use partially coherent on-chip holographic imaging geometries. In these geometries, light emitting diodes (LED) are preferred over lasers for illumination to avoid multiple reflections and speckle noise. Moreover, their compactness, low-cost, and durability make them ideal light sources for lensfree on-chip microscopy.

When the illumination source is not perfectly monochromatic, the recorded hologram is incoherent superposition of weighted monochromatic hologram intensities.

$$I_{\lambda_1} = \left|R_{\lambda_1} + S_{\lambda_1}\right|^2 = \left|R_{\lambda_1}\right|^2 + \left|S_{\lambda_1}\right|^2 + 2\mathrm{Re}\{R_{\lambda_1} S^*{}_{\lambda_1}\} \qquad (14)$$

$$I_{\mathrm{total}} = c_1 I_{\lambda_1} + c_2 I_{\lambda_2} + c_3 I_{\lambda_3} \ldots + c_i I_{\lambda_i} \qquad (15)$$

The spectrum of the illumination source and sensor spectral response curve defines the contribution (c) of each wavelength. This overlapping causes a smearing effect in the measured hologram, decrease the fringe visibility and cause all the high resolution information embedded within these fringes to be buried under background noise as represented in Figure 4. Another way to explain this is that the temporal coherency diameter shrinks as the source bandwidth (Δλ) gets wider.

$$\text{Coherence length}, L_c \sim \frac{\lambda \text{center}^2}{2\pi n \Delta\lambda} \qquad (16)$$

As a result, the lack of temporal coherence and artifacts due to the quasimonochromatic assumptions in recoveries of polychromatic holograms limits the maximum spatial resolution and cause artifacts as the source spectral bandwidth gets broader and broader. Although regular bandwidth of LEDs (~15nm) is mostly enough to provide a reasonable resolution for many biological objects, these limitations and artifacts become more pronounced as the spatial resolution demands get higher.

Some optical setup modifications can be considered to mitigate or at least reduce these limitations: using shorter wavelengths, closer object-sensor distances or narrowband spectral filters with LEDs. However these modifications cannot effectively address the need because of the following reasons: Common image sensors are not sensitive enough for lensfree imaging in very short wavelengths. Further reducing the object-to-sensor distance is not applicable for most of the sensor structures. Even so, it causes severe under-sampling of the holographic signatures, insufficient shifts for pixel super resolution, and lack of thermal isolation from the sensor chip, which is a significant issue for imaging live biological objects. Especially for conditions, which shorter object to detector distances and wavelengths are not applicable; narrowing the bandwidth of the source is the only solution to relax the temporal coherence limitation. Filtering high power LEDs by using narrow band (3-10nm, cost around $70-300) spectral filters works for high resolution imaging of static objects; although, it causes a very photon inefficient process and requires long image acquisition time. Thus, a computational solution is highly preferred to resolve artifacts due to the polychromatic nature of the LED illumination in lensfree imaging.

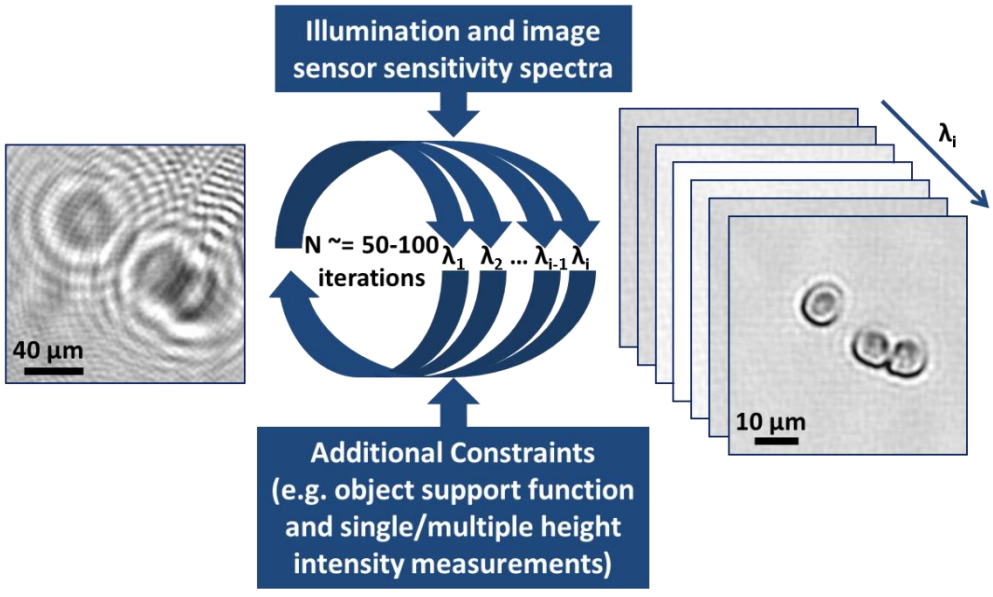

Figure 12: General Idea of Polychromatic phase retrieval (PolyPR)

To address this need, I use a polychromatic phase retrieval method (Figure 12, 13) to demultiplex the superimposed spectral characteristics of the object. This method partially relaxes the temporal coherence limitation without hardware restrictions and enables the use of illuminations with a wider spectral bandwidth. As a result, the improved light efficiency allows shorter image acquisition times and longer object-sensor distances. This algorithm iteratively converges into the complex multispectral field distribution by using the super-resolved polychromatic intensity measurement, source and detector spectra and additional constrains like rough spatial boundaries of the object of interest or multiple intensity measurements at different heights. It starts with the super-resolved intensity measurement, which is a weighted superposition of many monochromatic, in-line holograms. The weight factor for each wavelength is determined by the spectra of the illumination source and the sensor response. The initial hologram is scaled with each wavelength weighting factor and their square roots are propagated to the object level to enforce the object level constraint. Then the fields are propagated to the detector level, the total intensity is calculated and compared to the measured intensity to calculate the error. After enforcing the intensity level constraint, the fields are propagated back to the object level. Iterations continue up to 100 or as long as the mean square error is smaller than the previous iteration and the tolerance defined whichever happens first. Propagations in both directions are done by using angular spectrum method with i number of wavelength specific transfer functions.

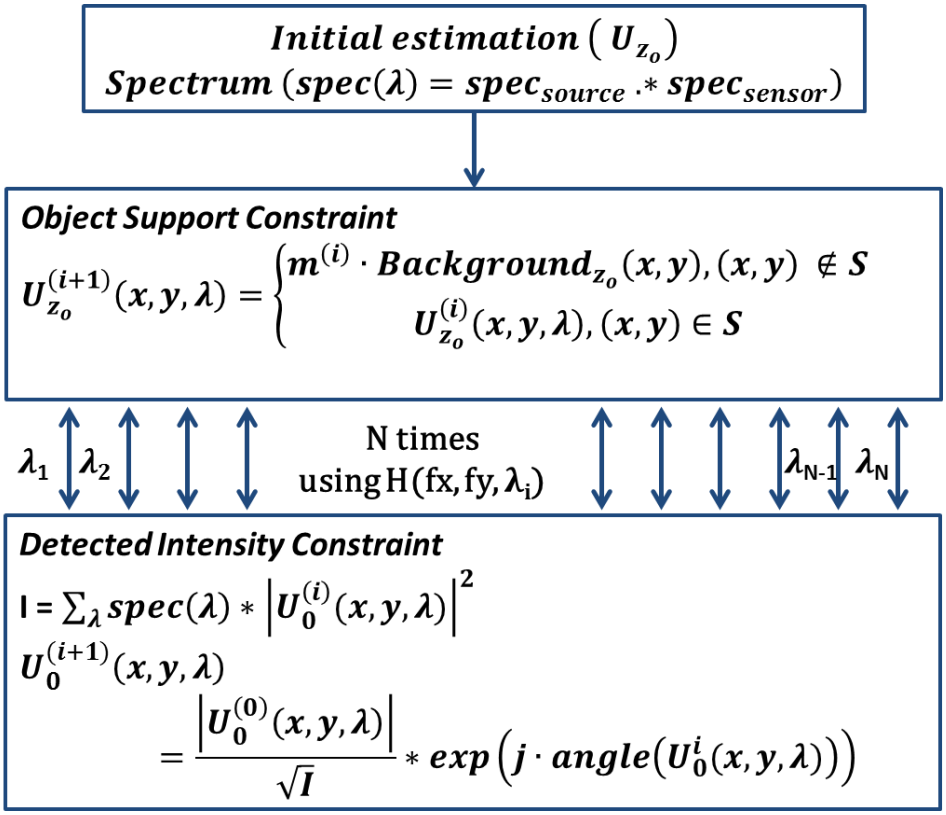

Figure 13: Details of the object support based Polychromatic Phase Retrieval approach used for lensfree holographic on-chip imaging

A similar approach was reported earlier for lensfree imaging using broadband X-ray sources which successfully reported 60 fold reduction in integration time by implementing polychromatic coherent diffraction imaging algorithm. [39] My method is different from the later in many ways. The first and most obvious difference is operating in the visible wavelengths and with on-chip geometry providing unit magnification inline holograms of the objects. I do not assume spectrally invariant objects, so I recover multispectral image cubes. I also do not use any the small angle and far-field assumptions, so instead of rescaling and interpolating, so I calculate each hologram per wavelength by using angular spectrum method. Initial estimation is the back-projection and it takes approximately 50-100 iterations to converge to the final recovery.

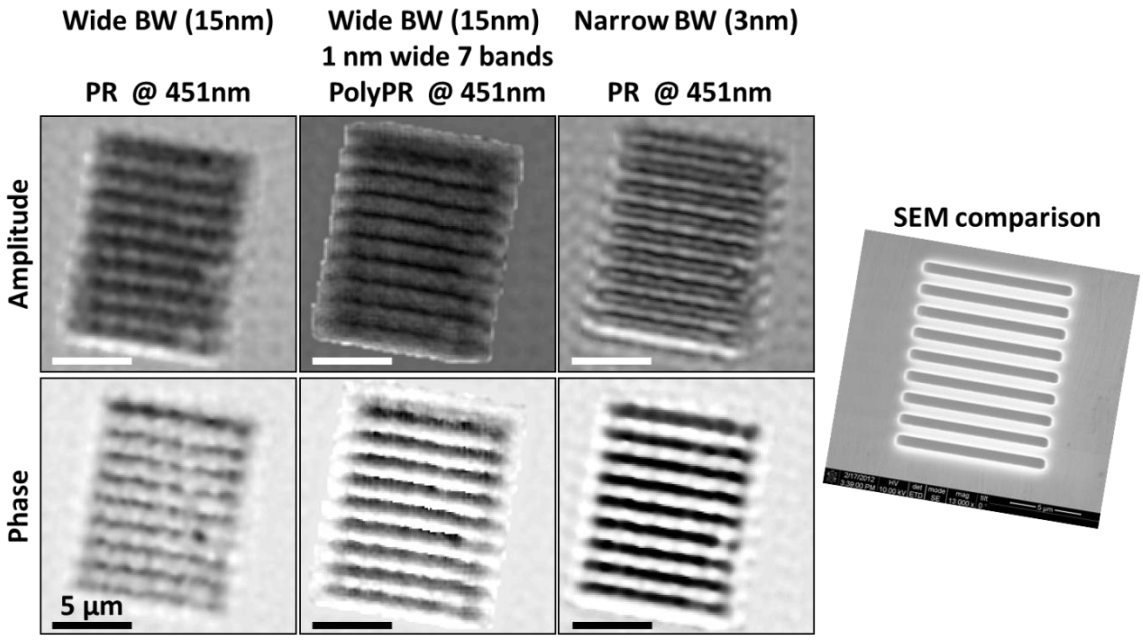

Figure 14: Modified Polychromatic phase retrieval (PolyPR) improves the resolution by relaxing the limitations due to the incorrect assumptions and lack of temporal coherency. Regular and polychromatic phase retrieval results from a 1.5µm-period grating hologram, which is illuminated with wide(15nm) and narrow(3nm) bandwidth (BW) LEDs compared against the SEM image of the grating

3.4 Portable Holographic On-Chip Imaging Platform Using Sunlight Illumination

Newton's experiments with a pair of prisms decomposed sunlight into its colors and combined it back to explain the refraction and dispersion of sunlight through a glass prism interface. Since this milestone experiment, the use of sunlight as a source in optical experiments continued to be quite common until other light sources such as incandescent light bulbs were invented. Providing us an easy-to-access and rather broad spectral content, the sunlight still presents a rich source that could potentially be used in multispectral imaging to extract the wavelength-dependent features of microscopic objects of interest. Along the use of broadband light sources for on-chip holography, I further demonstrate a field-portable, on-chip

platform performing color/multispectral imaging with white light and ultimately with sunlight illuminations over a wide field-of-view of e.g., 15-30 mm^2.

In this compact and light-weight partially-coherent holographic imaging geometry, the objects are placed at ~0.5 mm away from the active region of a color (RGB) CMOS sensor-array and are homogenously illuminated by the sunlight, which is first collected by a simple light collection unit adapted from conventional solar cell technologies. After trying some static collection approaches like wide angle lenses or compound parabolic condensers[40], I decided on a dynamic, angle scanning collection approach as seen in left of Figure 15, where I use a flexible light pipe (1mm diameter glass core).

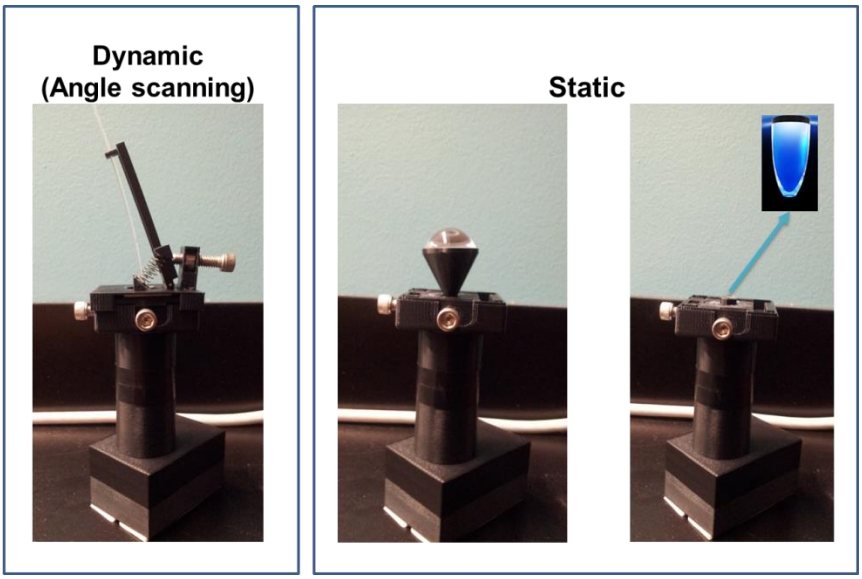

Figure 15: Some static and dynamic sunlight collection mechanism considered for the portable lensfree microscope unit.

I placed a plastic diffuser after the light pipe to prevent imaging the projection of the sky like a pinhole camera. After the sunlight passes through a plastic diffuser, it is spatially filtered by a 0.1 mm diameter pinhole/aperture. This pinhole is positioned at ~7.5cm away from the objects, and is controlled using a simple screw-based x-y translation stage, which permits capturing of slightly shifted in-line holograms of the objects. These lensfree images captured under sunlight are digitally combined using pixel super-resolution algorithms to form a finely

sampled in-line hologram per color channel (i.e., at red, green and blue channels). These pixel-super-resolved holograms are then processed with the knowledge of the spectral response curves of the sensor-array as well as the spectral content of the sunlight to digitally remove the cross-talk between color channels and retrieve the multispectral spatial features of the objects.

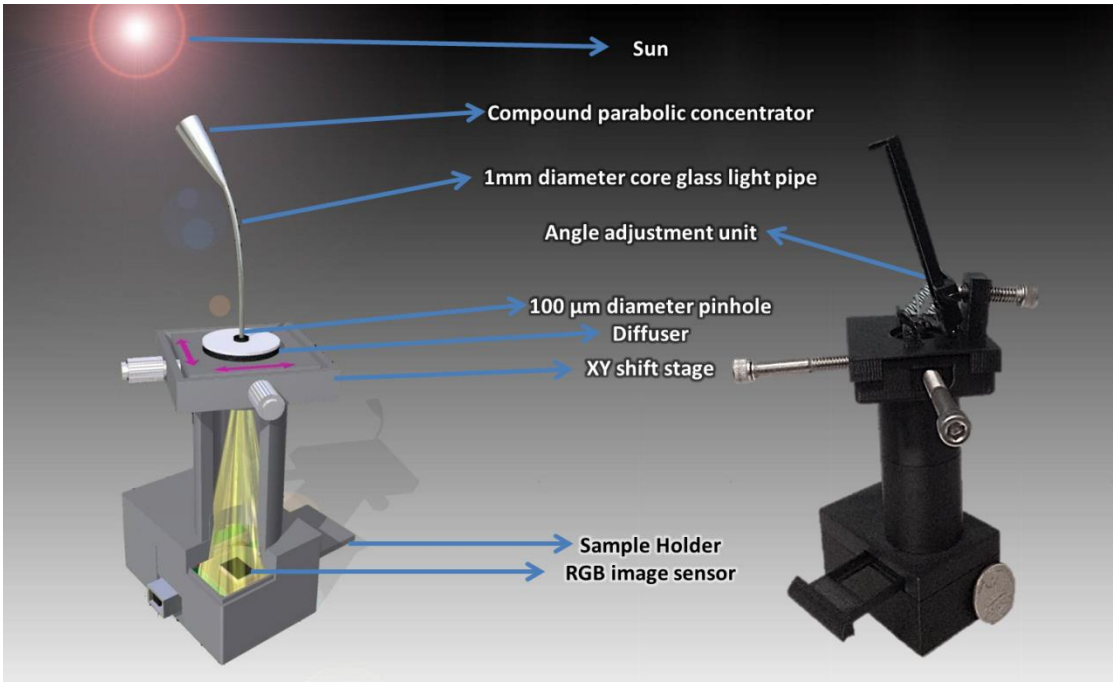

Figure 16: The field-portable lensfree holographic microscope using sunlight

Although spectral demultiplexing and phase retrieval for the on-chip holograms are addressing different problems, polychromatic phase retrieval introduced in previous section is a combined method performing both within a single recovery run for moderately wide illumination bandwidths. However when the source bandwidth is wider, as in sunlight, it is preferred to perform both these processes separately. For this end, instead of a polychromatic phase retrieval approach, I use a two-step recovery method for lensfree holograms recorded with sunlight illumination.

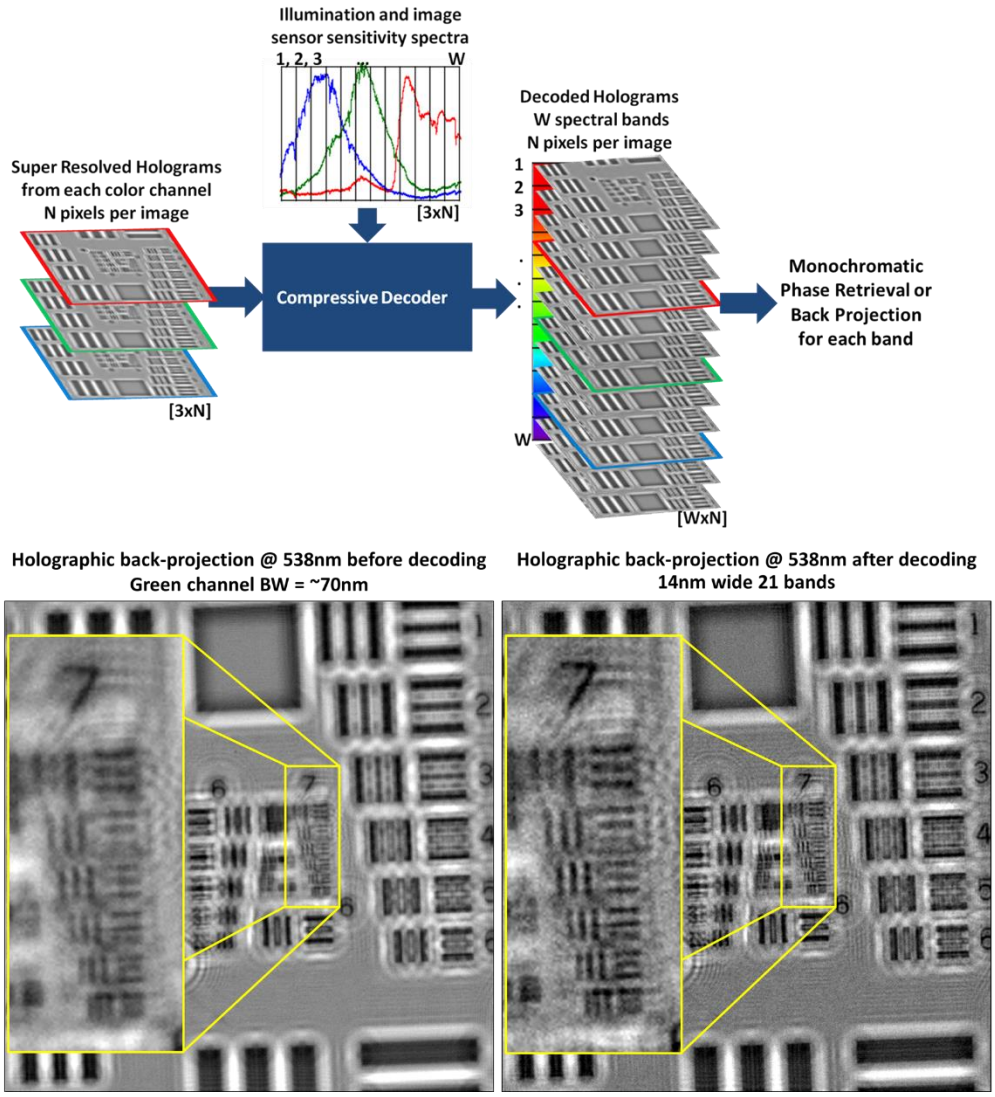

Figure 17: The redundant nature of the multispectral data is used to decode the sunlight holograms into narrower spectral bands.

The first step is the spectral demultiplexing method; where I estimate the weights of monochromatic holograms from super-resolved, polychromatic holograms at three color channels (red, green and blue). I approached this underdetermined problem with a compressive decoding method by using the knowledge of combined spectra of sunlight and sensor sensitivity since multispectral spatial data are naturally redundant. I minimize the squared l2 norm of the mismatch between the measurement and the estimation, regularized with the total variation of the multispectral object [30] Then the demultiplexed holograms are individually processed either

by using iterative monochromatic phase retrieval or a simple back-projection if the twin image noise is weak. In Figure 17, the recovery process is summarized (top) and the performance of the portable device is demonstrated (bottom) by using a US Air Force Resolution Target.

3.5 On-chip Sensing Platform Using Plasmonic Nano-apertures

After all these partially-coherent imaging applications of lensfree computational microscopy tools, I conclude this section with an on-chip, high-throughput platform for sensing applications. For this end, a microfluidic channel with plasmonic nano-aperture array at the bottom surface is demonstrated.[34] The system is illuminated by a partially coherent quasimonochromatic source (λ_{center} = 550 nm, 20 nm bandwidth), and the lensfree diffraction patterns of the metallic apertures are recorded by an optoelectronic sensor array (Figure 18-a). The spatial and temporal coherency diameter of the system is adjusted to be larger than each diffraction pattern; therefore the complex field after the apertures can be retrieved using the object support constraint. This field distribution is very sensitive to any refractive index change in the vicinity of the aperture arrays because of their plasmonic behavior. By cross-correlating these patterns through time, very fine refractive index changes can be sensed. Moreover the geometry of the setup allows to multiplex thousands of apertures simultaneously, making this system very suitable for high-throughput, label-free sensing applications. As a proof of concept, lensfree sensing of refractive index changes as small as $2x10^{-3}$ are experimentally demonstrated as illustrated in Figure 18-b.

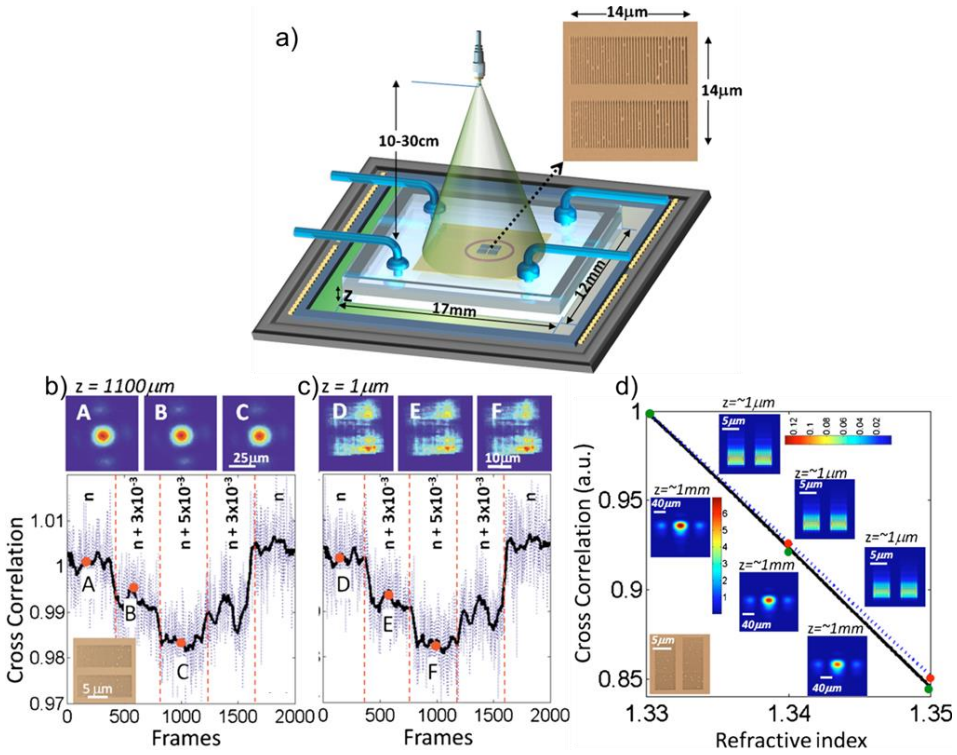

Figure 18: (a) Lensfree on-chip sensing setup. A plasmonic nano-aperture array, as shown in the SEM image, is illuminated with a quasimonochromatic source e.g., 550 nm center wavelength with ~20 nm bandwidth located 10–30 cm away from its surface. The lensfree transmission pattern of this plasmonic structure is sampled by a CMOS chip placed at z=~1 mm away from the aperture plane. The yellow surface indicates the detector active area (6.4 mm^2). The plasmonic nano-aperture array shown above is composed of uniformly spaced slits each with a length of 6 µm where the slit width varied -from left to right- between 80 and 200 nm in discrete steps of 20 nm. The physical gap between two neighboring slits is kept constant at ~200 nm. Cross correlation coefficients are calculated between the first lensfree transmission pattern and the subsequent patterns for the detector plane (z=1100 µm) (b) and the reconstruction plane (z=1 µm) (c), as illustrated with the blue dotted lines. The same plots also show the running averages of these cross correlation coefficients over 50 frames as shown with the black solid lines. The intensities of the lensfree transmission patterns used in these graphs are normalized to the instantaneous illumination intensity, which is also detected using the same CMOS chip through a large aperture. The initial refractive index of these sensing experiments (n) is 1.333 corresponding to DI water. Top row: A-C illustrate the raw lensfree diffraction patterns of the nano-aperture array at three different refractive indices within the microfluidic channel n, n+3x10^{-3}, and n+5x10^{-3}, respectively, where all the lensfree transmission patterns extend over a width of ~50 µm. Top row D-F illustrate the reconstructed transmission patterns of the same nano-aperture array at z=1 µm plane, right underneath the aperture region. (d)The cross-correlation coefficients vs. refractive indexes calibration of system based on Fourier Domain Time Domain (FDTD) simulations for lensfree transmission patterns at z= 1mm (solid line) and at z=1µm. [34]

3.6 Discussion

In Chapter 3, partially coherent imaging and sensing applications of lensfree holographic microscopes, which all use visible wavelengths, are reported. A next step in this direction is transferring benefits of lensfree on-chip holographic imaging to long infrared wavelengths. Thermal range of the electromagnetic spectrum is very valuable for security and quality inspection applications since it allows imaging with objects and settings like visibly dark, turbid, scattering, or even opaque mediums, which visible light cannot be effectively used for.[1]–[4]. Therefore, developing a lensfree holographic imaging platform operating at long-infrared wavelength range is highly desirable.

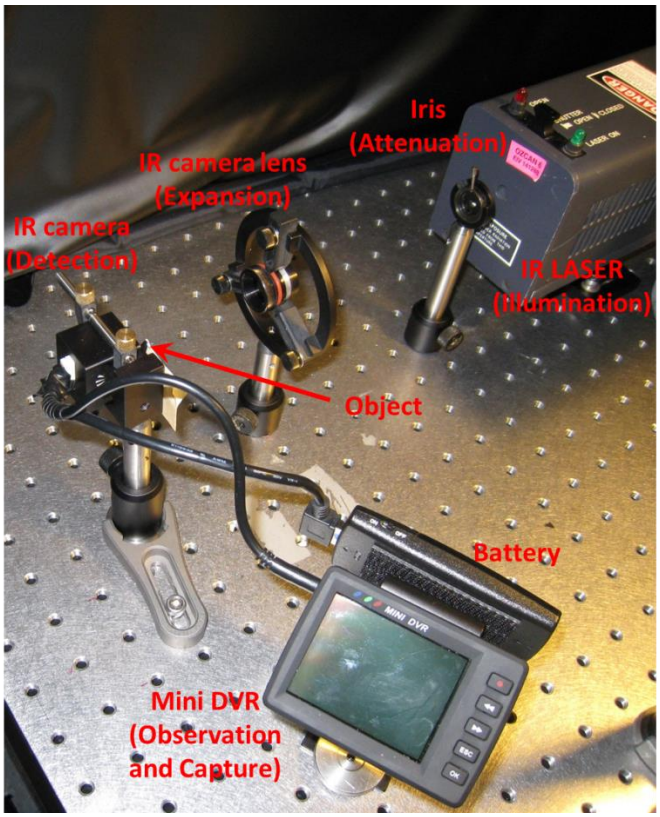

Figure 19: Lensfree long-infrared holographic imaging setup

For this end, I construct a basic setup shown in the figure above with an IR camera (DRS Infrared, Tamarisk™ $_{320}$) and a continuous wave CO_2 laser (λ = 10600nm). The iris in front of the laser aperture serves to attenuate the laser beam whereas the IR camera lens

focuses and then expands the beam for the camera sensor. Object is placed immediately in front of the detector of the camera (z_2 <1.5cm). Active area of the camera is 240x320 pixels with 17 micrometer pitch size. Output images of the camera are 600x800 pixels with 6.8 micrometer pixel size. I performed a proof-of-concept experiment with a metallic needle tip to show the performance of this platform. The raw hologram, the backprojected object amplitude and phase images are reported in Figure 20.

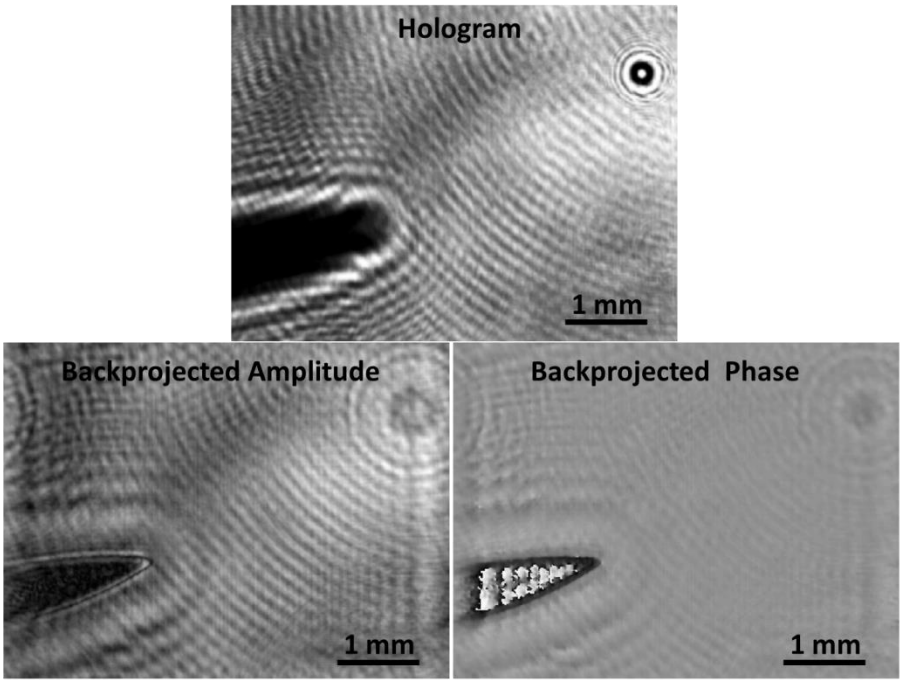

Figure 20: Lensfree raw hologram of a metallic needle tip recorded with the setup shown in Figure 19 (top) and its backprojected amplitude and phase images.

With the implementation of pixel super resolution based on object shifting, this platform can achieve diffraction-limited spatial resolution, and be used for applications like volumetric micrometer scale defect analysis of opaque objects.

After the working principles and applications of the partially coherent imaging/sensing tools are discussed in Chapter 3, Chapter 4 is focused on the incoherent lensfree imaging platforms (FLUOCHIP and MONA).

Chapter 4 Lensfree Incoherent Imaging Applications

The methods and applications reported in this chapter are already published as journal articles in the following references:[5], [14]–[16], [41], [42], [43]

In the former chapter, I report several computational microscopes, which are working based on partial coherence of their illumination sources to perform imaging and sensing by mostly using holography. There are also biomedical applications involving fluorescent imaging, which can greatly benefit from computational microscopy methods to achieve ultra-wide field of view (FOV), high-resolution, on-chip fluorescent imaging with lower complexity and cost compared to conventional approaches. In this section, I introduce incoherent, computational microscopy platforms designed to achieve this goal. These lensfree imaging platforms have the potential to optimally serve for large area of applications, that each has different requirement levels in throughput, spatial resolution, and structural simplicity. I report five different applications of two main incoherent computational microscopy techniques: **FLUOCHIP** (**F**luorescent, **L**ensfree, **U**ltra-wide field-of-view, **O**n-**C**hip, **H**igh-throughput **I**maging **P**latform) and **MONA** (**M**icroscopy with **O**n-Chip **N**ano-**A**pertures). These applications are presented in a flow that the main objective of the imaging platform shifts from maintaining ultra-wide field-of-view with structural simplicity towards maintaining high throughput with higher spatial resolution.

4.1 Fluorescent, Lensfree, Ultra-wide field-of-view, On-Chip, High-throughput Imaging Platform (FLUOCHIP)

Before the applications, the basic working principle of FLUOCHIP can be summarized as follows: As illustrated in Figure 19, the fluorescent samples within a micro-channel are illuminated by using a rhomboid prism which allows coupling the light into the channel over a wide area with a fairly uniform power distribution. After this incoming light excites the sample, the excitation light and some portion of scattering light have been rejected by the total internal

reflection (TIR) occurring at the air glass interface of the bottom cover slip. While the fluorescent emission transferred onto the sensor array, leftover scattered light absorbed by the 30-100µm thick absorption filter placed right before a charge coupled device (CCD) or a complementary metal oxide semiconductor (CMOS) sensor without the use of any lenses, thin-film interference filters or mechanical scanners. This compact design enables to use the entire sensor active area as an ultra-wide imaging field-of-view (FOV) as shown in Figure 19.

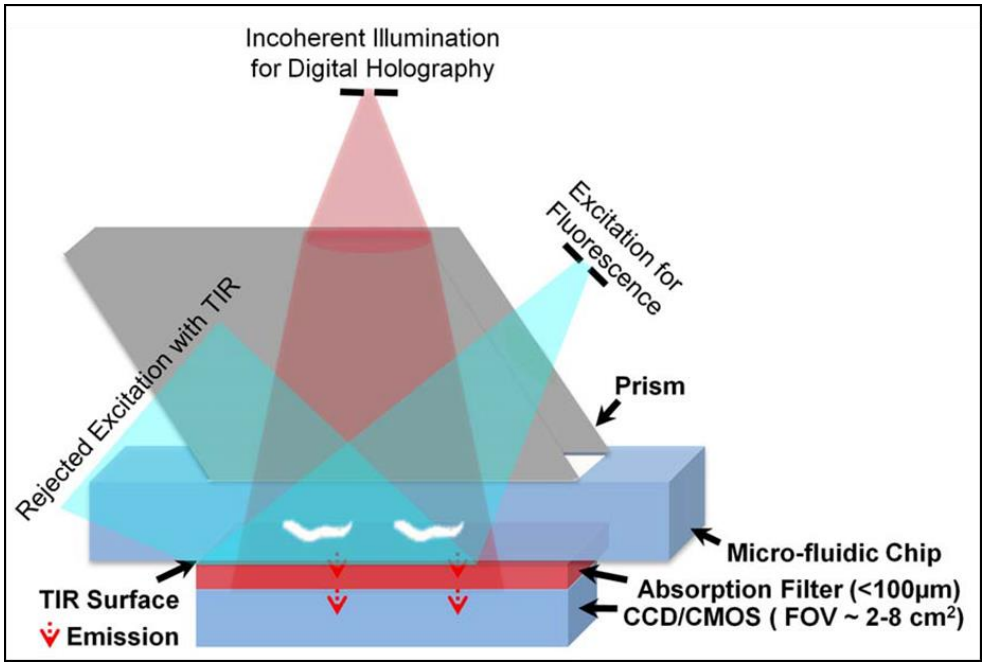

Figure 21: Schematic of FLUOCHIP with dual mode (fluorescent and holographic) imaging capability. Fluorescent excitation is achieved through the side facet of a rhomboid prism using an incoherent source (i.e. spectrally filtered Xenon lamp); and holographic illumination is achieved through the top facet of the same prism using an Light Emitting Diode (LED) (632 nm peak wavelength and 20 nm spectral bandwidth)[42]

Before any processing on raw lensfree fluorescent images, there is a need to know the response of the system to an incoherent point source located at a constant height within the object chamber, namely the point spread function (PSF). This space-invariant PSF of the system is determined experimentally, by aligning and averaging statistically enough number of isolated signatures from very small diameter fluorescent beads. Since the lensfree fluorescent detection occurs at extremely oblique angles on the sensor chip, depending on the opto-

electronic design of the pixels and the underlying circuitry of a given chip, the fluorescent point-spread functions (PSF) would exhibit a noticeable variance in its 2D pattern from one sensor-chip to another, which requires calibration of each chip by measuring its unique PSF. Because fluorescent emission rapidly diverges, such raw fluorescent images recorded on a chip look blurred due to broad point-spread-function of this lensfree platform. To combat this resolution challenge, I used optimization based on a compressive sensing algorithm[44], [30] to decode the recorded lensfree fluorescent patterns into higher resolution images.

$$f(x) = (1/2)\|y - Ax\|_2^2 + \lambda\|x\|_1 \qquad (17)$$

This approach can be understood as a simultaneous multicolor deconvolution operation with additional sparsity constraint. 'A' here represents the forward model of the system, y is the raw measurement, λ is the regularization parameter and the x is the estimated object distribution. More specifically, in this cost function I minimize the mismatch between the measured and estimated values, which is regularized by the l1-norm of the object. This regularizer is assuring the convergence to a sparse solution. Compressive decoding of raw lensfree images (using the measured PSFs) permits close to an order-of-magnitude increase in the resolving power by rapid digital reconstruction of the fluorescent distribution at the object. The performance of this compressive decoding approach is quantified in Figure 21 (for KAF-8300 and KAF-39000 chips, respectively), which both indicate a resolution of ~10 μm that is independently confirmed using conventional fluorescent microscope images of the same 4μm particle pairs (Figure 21, inset). These experimental results successfully demonstrate the sensor-chip independent decoding performance of the lensfree fluorescent imaging platform.[42]

The resolution limit in this lensfree imaging results is mainly dictated by the detection signal-to-noise-ratio (SNR), since the tails of the measured PSF, after certain signal strength, fall below the noise floor of the sensor. In these reported experiments (Figure 20) the CCD chips

were kept in room temperature, and therefore further improvement in resolution (beyond ~10μm) can potentially be achieved by active cooling of the opto-electronic sensors without a trade-off in the imaging FOV, which spans the entire active area of the CCD, i.e., ~2.4 cm^2 for KAF-8300 and ~8 cm^2 for KAF-39000 (Figure 20). It also should be noted that, with larger area sensors, the imaging FOV of this platform can be even further increased while maintaining a similar resolution level.

On a related note, it is important to emphasize that the pixel size in lensfree compressive imaging is “not” a fundamental limitation for spatial resolution if the detection SNR is sufficiently high. Considering lensfree imaging of two fluorescent points that are directly located on a single pixel. Under this condition, it is theoretically and practically impossible to resolve these two fluorescent points that fall within a single dummy pixel. However, the same two sub-pixel fluorescent points can be resolved from each other using lensfree compressive imaging if several pixels could detect weighted averages of their fluorescent emission. Therefore, under an appropriate detection SNR, if the physical gap between the fluorescent objects and the sensor plane can be increased to perform efficient spatial encoding of the fluorescent objects, resolving of arbitrarily sub-pixel point sources would be feasible. The fundamental limitation to this resolving power is therefore the detection SNR, which determines how many pixels can independently and accurately measure the lensfree fluorescent contributions of the particles. Therefore, for a practical SNR level, there is always an optimum gap range between the object and sensor planes, which is optimized to be ~50–200 μm for the CCD chips at room temperature.

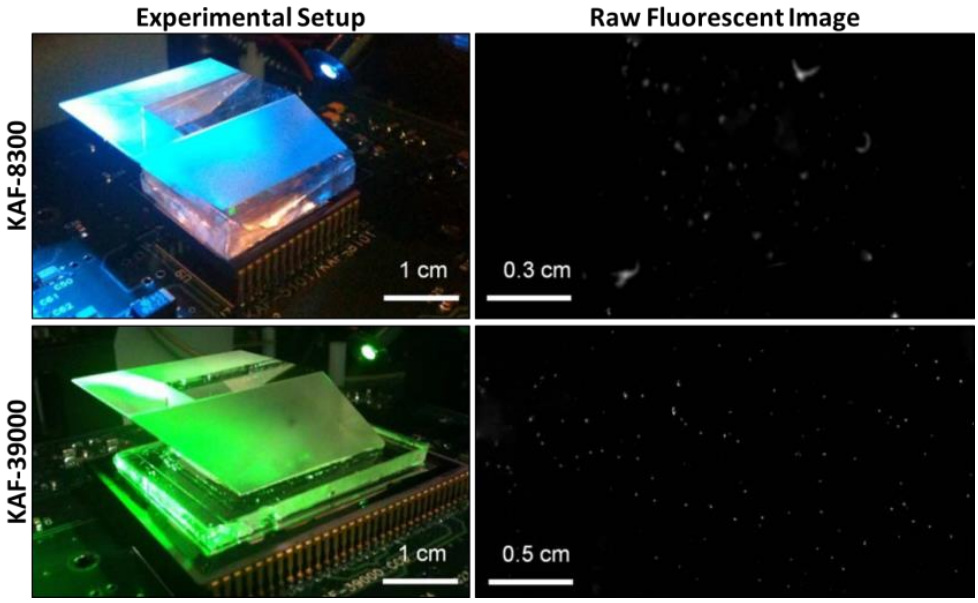

Figure 22: Lensfree fluorescent imaging is demonstrated over 2 cm^2 using KAF-8300 sensor (Full Frame CCD with pixel size of 5.4 µm) and over 8cm^2 using KAF-39000 sensor (Full Frame CCD with a pixel size of 6.8 µm). The fluorescent C. elegans samples were excited through a prism interface as shown in the experimental setups, where index matching oil was used to assemble the chip and the prism. Only the fluorescent emission emerging from gene-expressed parts of the worm body is detected by the sensors.[42]

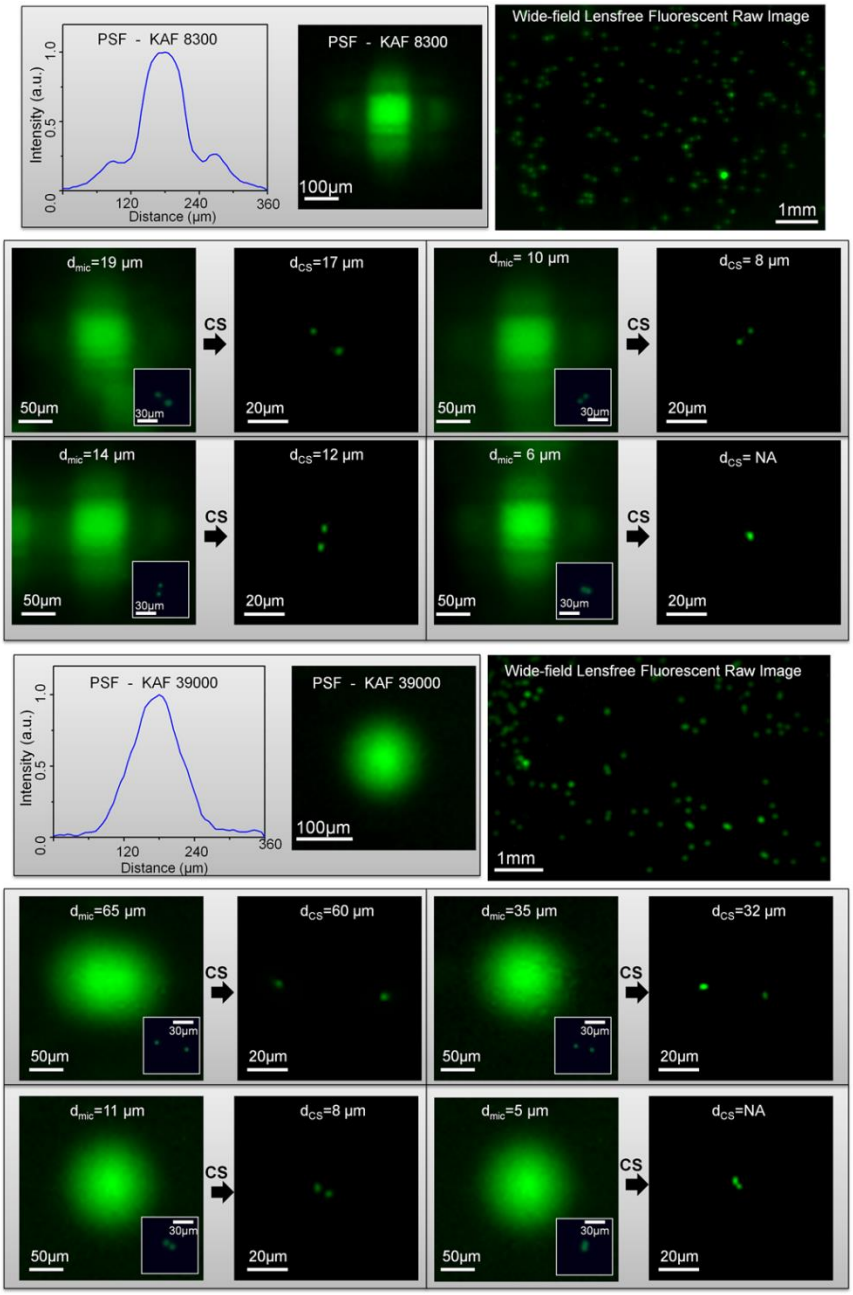

Figure 23: Wide-field lensfree fluorescent imaging results for 4 μm fluorescent beads recorded using KAF-8300 and KAF-39000 sensor chips. The point-spread-function (PSF) crossections of the systems are also shown at the top left for each CCD type. (Middle and Bottom Rows) Lensfree fluorescent images of various 4 μm bead-pairs are shown, the inset images in each frame also show conventional fluorescent microscope images of the same closely-packed beads for comparison. The center-to-center distances (d_{mic}) between the fluorescent particles are calculated based on these microscope images. Using compressive sampling (CS), lensfree fluorescent raw images are decoded to resolve the individual fluorescent particles. These decoding results nicely match to the corresponding microscope comparison images for $d_{mic} \geq 10\mu m$. d_{CS} refers to the center-to-center distances of these resolved fluorescent particles in the decoded lensfree images.[42]

After this resolution discussion, the first application of FLUOCHIP reported in this chapter is lensfree, on-chip fluorescent imaging of transgenic Caenorhabditis Elegans (C. elegans) worms. C. elegans is an important model organism that has been widely studied in various fields such as genetics, oncology, and neurobiology. Wide-field optical imaging of C. elegans is an essential need for all these fields to enable high-throughput screening of this model organism. While several high-throughput imaging platforms have been successfully demonstrated so far, the main stream for this application involves the use of lens-based conventional optical microscopes which can only provide a limited field-of-view (FOV) of e.g., ≤1mm^2, and therefore require mechanical scanning to provide a larger imaging FOV. In addition to this, such conventional optical microscopy platforms are rather bulky, and do not provide a decent match in terms of compactness to micro-fluidic technologies that are becoming widely used today in high-throughput screening of C. elegans. With this alternative on-chip approach proposed here, for the first time that a lensfree, on-chip platform has successfully imaged fluorescent C. elegans samples over such an ultra-wide FOV. The sparse nature of the genetic expressions allowed compressively decoding the objects without representing them in any sparsifying basis and achieving the spatial resolution around of 10µm.

As shown in Figure 22, raw lensfree fluorescent signatures of the worms are highly blurred due to the broad PSFs. However, using the measured PSF of each platform, these lensfree signatures can be compressively decoded to digitally yield much higher resolution images of the fluorescent regions located within the C. elegans body, which very well agree with the images obtained using a regular lens-based fluorescent microscope. These experimental results successfully demonstrate the efficacy of the compressive decoding approach to image transgenic C. elegans samples using lensfree fluorescent on-chip imaging over an ultra-wide FOV that covers the entire active area of the CCD chip (e.g., >2–8 cm^2).

FLUOCHIP can also perform sequential bright-field imaging of the same samples using partially-coherent lensfree digital in-line holography that is coupled from the top facet of the same prism used in fluorescent excitation as shown in Figure 19. This unique combination permits ultra-wide field dual-mode imaging of C. elegans (Figure 22, f) on a chip which could especially provide a useful tool for high-throughput screening applications in biomedical research.

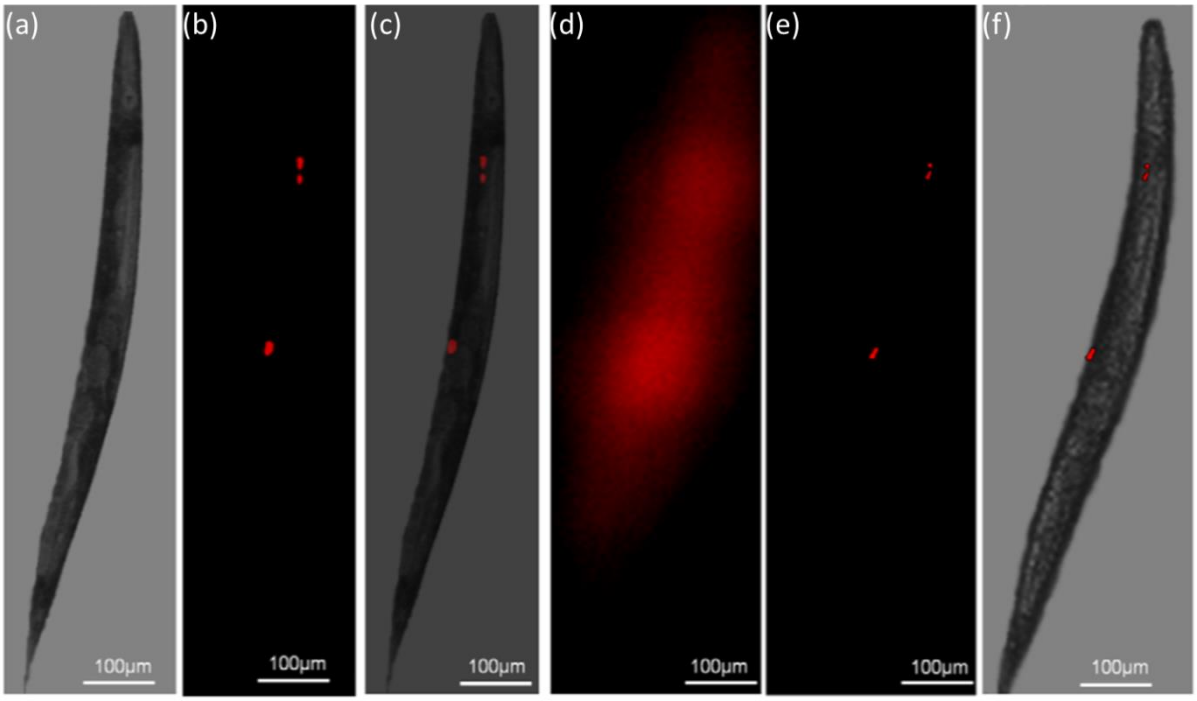

Figure 24: Lensfree fluorescent and holographic transmission imaging of C. elegans is shown for an individual animal using KAF-8300 sensor. (d) illustrates the lensfree raw fluorescent image that all looks blurry at the detector plane. Compressive decoding of these blurry patterns enabled digital reconstruction of much higher resolution fluorescent image of these C. elegans sample as shown in (e). 10X objective-lens fluorescent microscope images of the same worm shown in (b) agree well with the decoded lensfree fluorescent image. In addition to fluorescent imaging, the same lensfree platform also permits holographic transmission imaging of the same sample such that a hybrid image can be created by superimposing the decoded lensfree fluorescent image and the reconstructed holographic image as shown in (f). Microscope comparison of the same sample is also provided in (a) Slight rotation of the worm is observed between the lensfree decoded image and its microscope comparison image since they are acquired at different experiments.

4.2 Color-FLUOCHIP

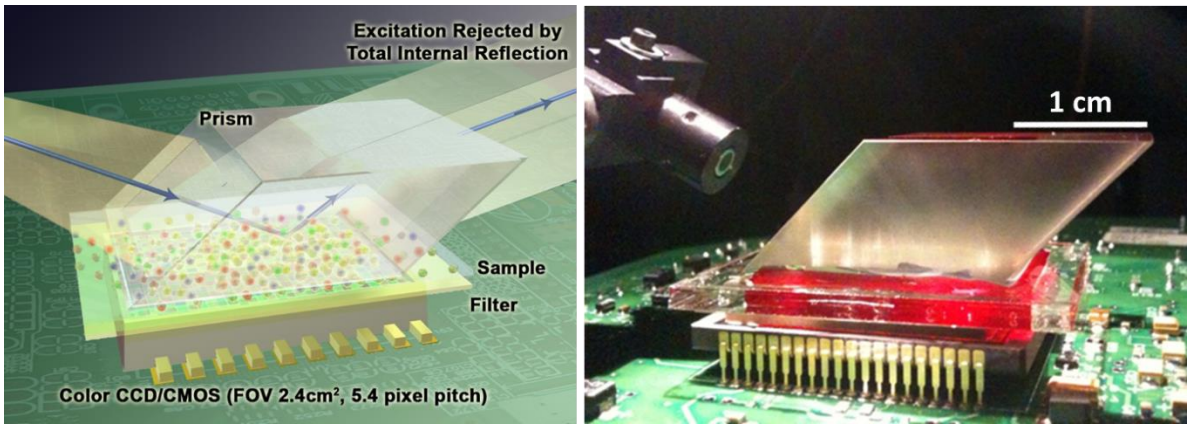

Figure 25: Lensfree, on-chip multicolor fluorescence cytometry platform

This subsection is on how to achieve simultaneous multicolor fluorescent cytometry on a chip. Performing fluorescence detection without lenses by using on-chip geometry can provide extreme throughputs as discussed in previous section. Further increasing the multiplexing capabilities and specificity of the on-chip fluorescent cytometers by performing simultaneous multicolor detection is highly desirable. For this end, I preferred to use a color sensor (KAF-8300 RGB CCD with 5.4µm pixel pitch), and then experimentally characterized the red, green and blue point spread functions of the imaging system with smallest observable fluorescent micro-particles. The measured fluorescent intensities from multiple isolated particles are interpolated, aligned, and averaged, as done for single color signatures. These intensity profiles depend on the structure of the sensor, filter response and the distance between the particles and the detector. The point spread functions for each color channel and the Bayer pattern arrangement type of the sensor are used to decode the color and high resolution spatial distribution of the fluorescent emitters from a single raw image by using the same optimization used for single color signatures. However, this time I modified the forward model to take into account different PSFs for different colors, down-sampling due to the large pixel size and the Bayer pattern type, in other words the distribution of the pixel color filters. Figure 24 summarizes color FLUOCHIP recovery process.

In this recovery process, sparsity is particularly effective as an additional constraint while processing lensfree fluorescent cytometry data since the object distribution in spatial and color domain is already sparse without any additional domain representation. However this logic can be easily extended into various imaging applications, since almost all of the natural and manmade objects of interest can be sparsely represented.

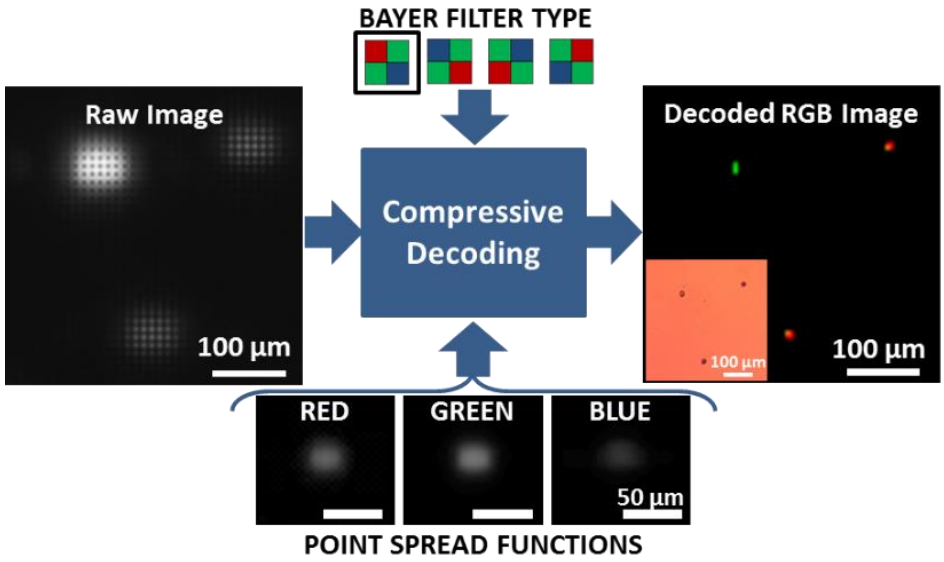

Figure 26: Lensfree, simultaneous multicolor fluorescence cytometry based on sparse signal recovery using the system point spread function and sensor spectral response information

The performance of simultaneous on-chip color imaging approach is tested with 4 µm green fluorescent beads and 10 µm red and green fluorescent beads as shown in Figure 25. The raw signatures were corrupted with the Bayer pattern artifact and severely overlapped and due to the lensfree nature of the platform. The color of the objects and their spatial distribution are successfully recovered and verified with fluorescent and bright field microscope images. This simultaneous multicolor imaging feature further boosts up the throughput and multiplexing capability of FLUOCHIP. This unique platform with its extreme throughput can be very useful for applications like biological assays, high volume rare event screenings, and imaging cytometry.

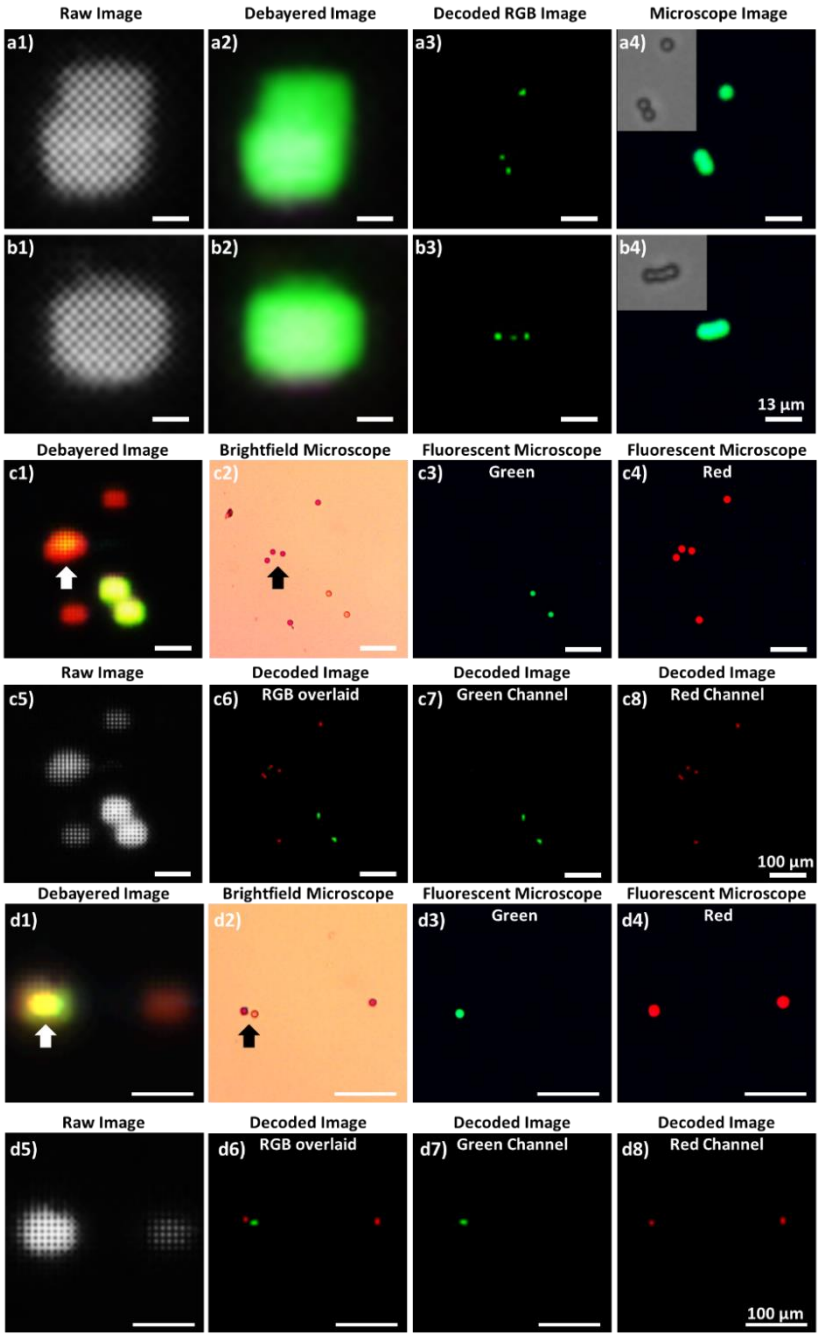

Figure 27: Raw, lensfree fluorescence signatures of microbeads are cropped from an extremely wide field-of-view of ~2.42 cm^2. They are decoded to achieve color and high-resolution spatial distribution information. Decoding results are verified with regular or fluorescent microscope images. The debayered images are showing the limit of the color sensor before the demultiplexing. a, b) Decoding results for 4 µm green fluorescent beads compared against bright-field (a4 and b4 insets) and fluorescence microscope images (a4 and b4). c, d) Decoding results for 10 µm red and green fluorescent beads compared against bright-field (c2 and d2) and fluorescent microscope images (c3,c4 and d3,d4). The arrows are highlighting two regions, where the decoding method effectively resolves the spatial and color overlapping issues of lensfree fluorescent signatures.

4.3 FLUOCHIP with Fiber-optic Faceplates and Tapers

The next FLUOCHIP implementation is designed to further improve of the system and make it better suit for applications like high-throughput cytometry, micro-array imaging, and rare cell detection, e.g. circulating tumor cells. For this end, a fiber-optic faceplate is added between the bottom end of the object chamber and the detector as shown in Figure 26.

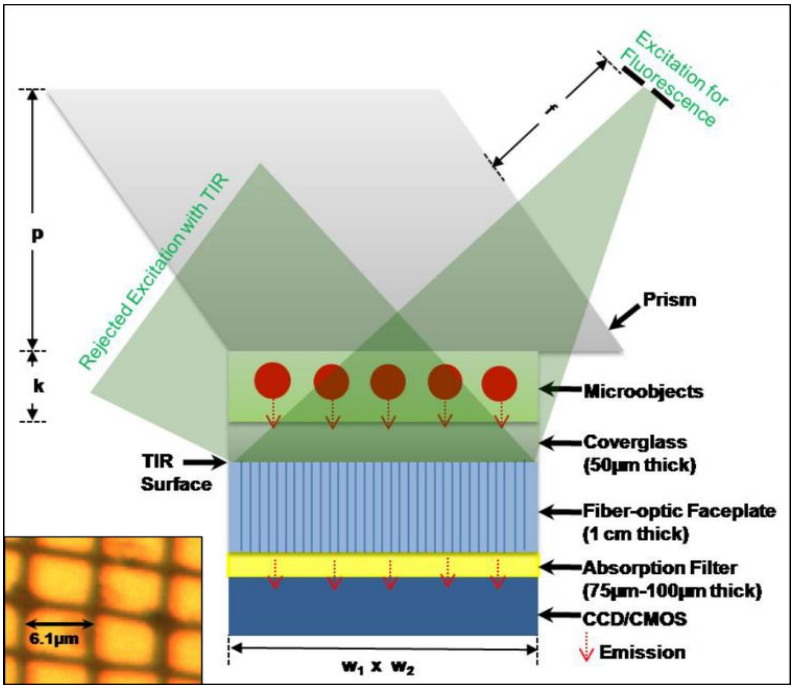

Figure 28: Schematic diagram of the lensfree on-chip fluorescent imaging platform is shown. Drawing is not to scale. This imaging platform has unit magnification such that the imaging field-of-view equals to the entire active area of the sensor array (i.e., >8 cm^2). The Total Internal Reflection condition occurs at the glass-air interface at the bottom facet of the coverglass. To avoid detection of scattered pump photons a plastic absorption filter is used after the faceplate. Typical dimensions: w1 x w2 = 25mm x 35mm; p = 1.7 cm; k =10-100 μm; f = 1-2 cm. (Inset) The microscope image of the faceplate is shown in the left bottom. The numerical aperture of each fiber is ~0.3. [5]

This dense bundle of fibers provided several advantages: It provided the thermal and mechanical isolation of the objects from the very proximity of the sensor which is an important advantage while working with sensitive objects like living cells. It also increased the signal-to-noise ratio (SNR) of the system by narrowing down the PSF. Although this narrowing behavior reduced the incoherency between sampling and sparsifying bases; it also increased SNR

significantly simplified the decoding problem by narrowing down the PSF of the system. As a result, spatial resolution of 10 µm even with a larger pixel size of 9µm is achieved. [5]

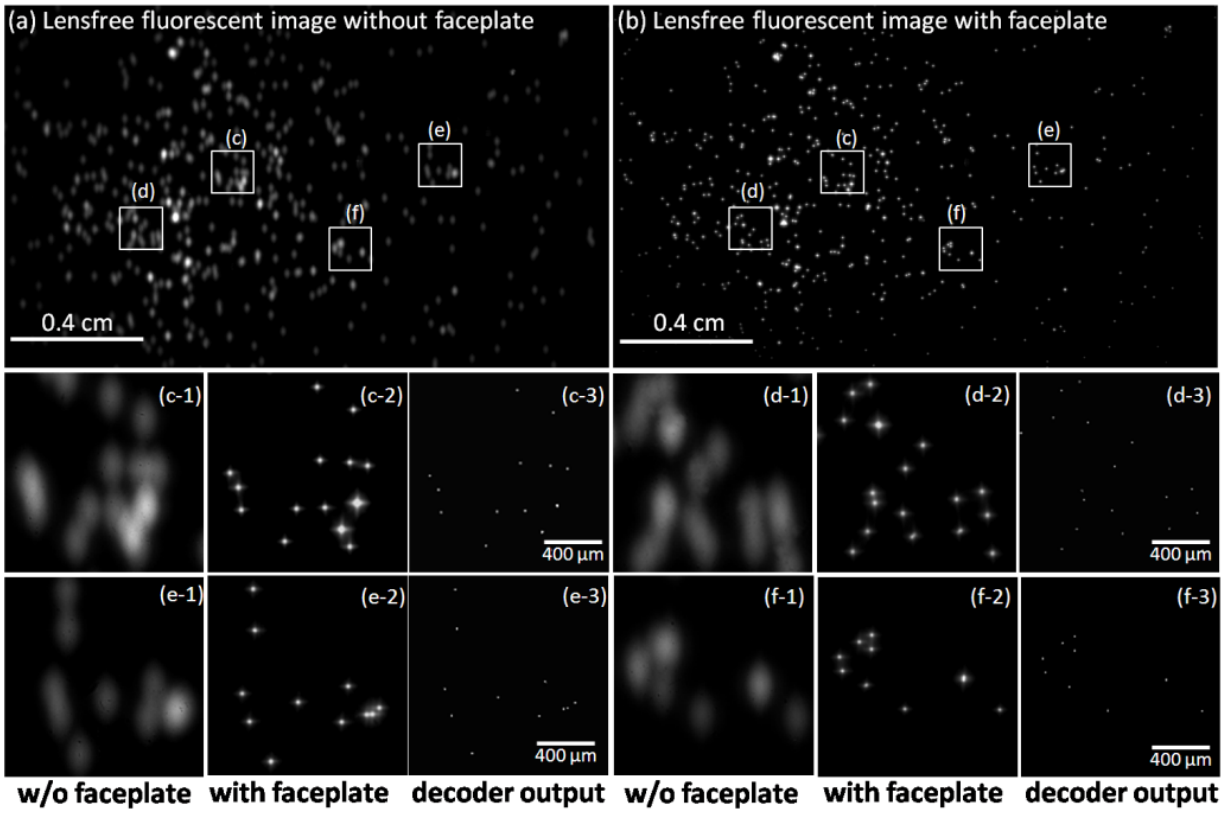

Figure 29: (a-b) Lensfree fluorescent images of 10 µm particles are compared with and without the faceplate. With the use of the faceplate, the spatial spreading of the fluorescent signatures at the CCD plane is reduced from ~180 µm down to ~36 µm (FWHM). This improvement is also evident in the comparison that is provided by the digitally zoomed regions shown in (c1-f1) and (c2-f2), which correspond to experiments “without the faceplate” and “with the faceplate”, respectively. The same zoomed images of (c2-f2) are also decoded using a compressive sampling algorithm to yield (c3-f3). [5]

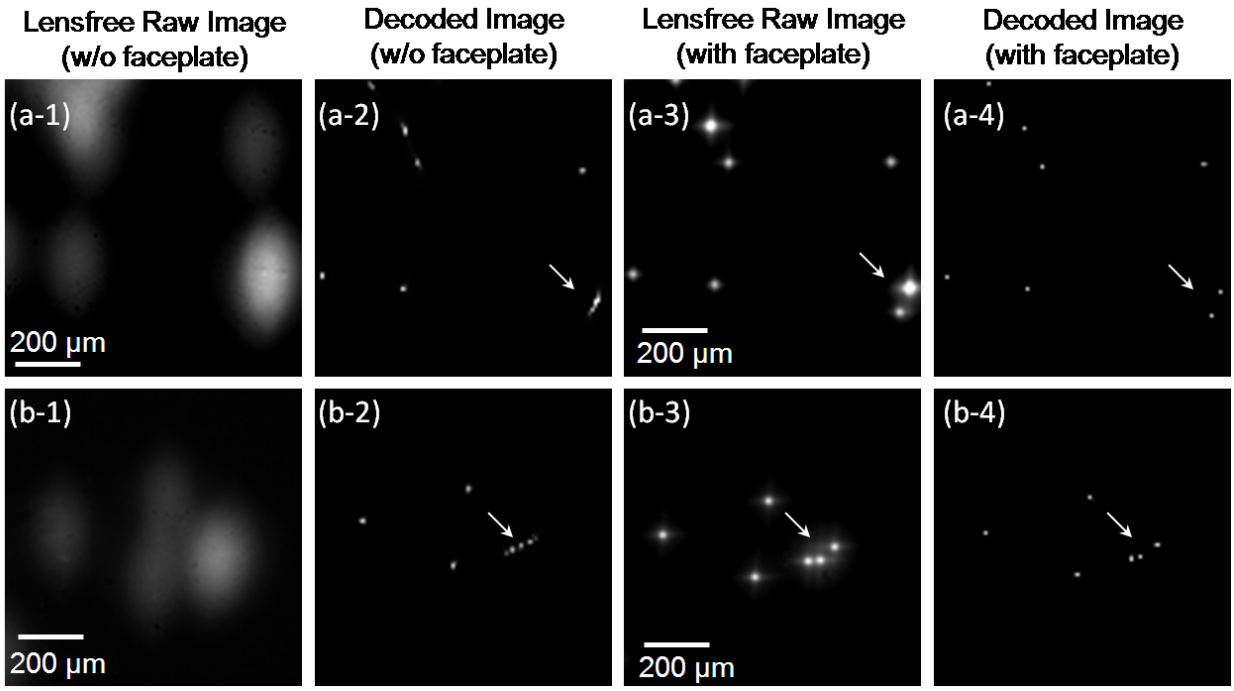

Figure 30: (a1) shows a digitally zoomed lensfree fluorescent image of 10µm particles that is obtained without the use of a faceplate. (a2) illustrates the output of the compressive decoder for the same image in (a-1). (a3) shows the same region of interest imaged this time using a faceplate as shown in Fig. 1(a). The compressive decoder output of image (a3) is shown in (a4). The same story is repeated in (b1) through (b4) for a different region of interest. The arrows in these images specifically point to regions where the improvement due to the faceplate becomes apparent to better resolve closely spaced fluorescent particles.

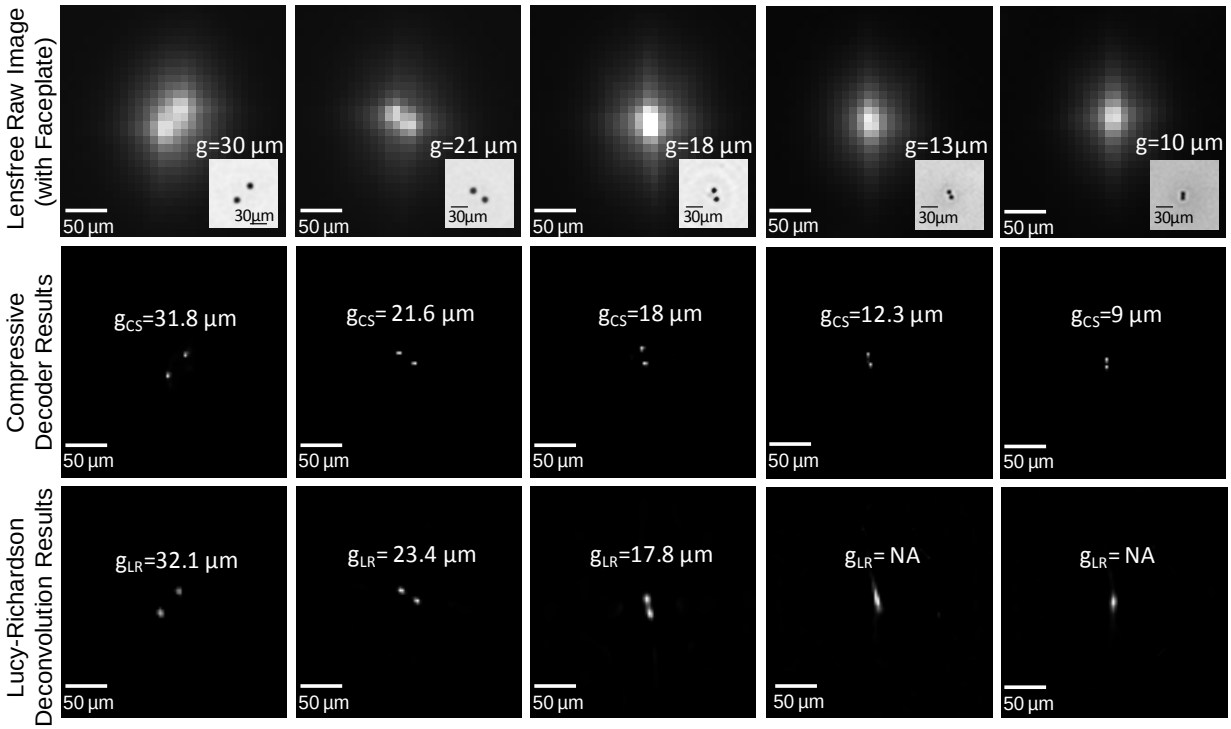

Figure 31: (Top Row) shows raw lensfree fluorescent images of different pairs of 10 µm diameter particles imaged using the set-up of Figure 26. As the particles get closer each other, their signatures in the raw lensfree image become indistinguishable to the bare eye. The inset images in the top row (bottom right corner of each image) illustrate transmission microscope images of the same particles from which the center-to-center distance (g) in each case is calculated only for comparison purposes. (Middle Row) illustrates the results of the compressive decoding process for each lensfree image of the top row. g_{CS} refers to the center-to-center distance of the resolved fluorescent particles in each image, where CS denotes "compressive sampling". Even for g = 10µm case (far right column), the fluorescent particles are clearly resolved from each other with g_{CS} = 9µm. The pixel size in the decoded image is 3µm, whereas the raw lensfree image has been sampled with a pixel size of W = 9µm at the detector array, i.e., N = 9M. The reason that the reconstructed points for g_{CS} = 9µm case do not touch each other (unlike the microscope image shown in the inset) is that the incoherent point-spread function of the system has been estimated using 10µm diameter fluorescent particles. The computation times of these decoded images vary between 0.1 min to 0.5 min on an Intel Centrino Duo Core, 1GHz PC. (Bottom Row) illustrates the deconvolution results of the Lucy-Richardson algorithm for the same set of lensfree images shown in the top row. g_{LR} refers to the center-to-center distance of the resolved fluorescent particles in each image, where LR denotes "Lucy-Richardson". The number of iterations in these deconvolution results ranged between 200 and 400, matching with the overall computation time of the CS results for each image. These results indicate that the LR algorithm can resolve particles with g~18 µm, whereas the CS decoder can clearly resolve particles with g~10 µm.

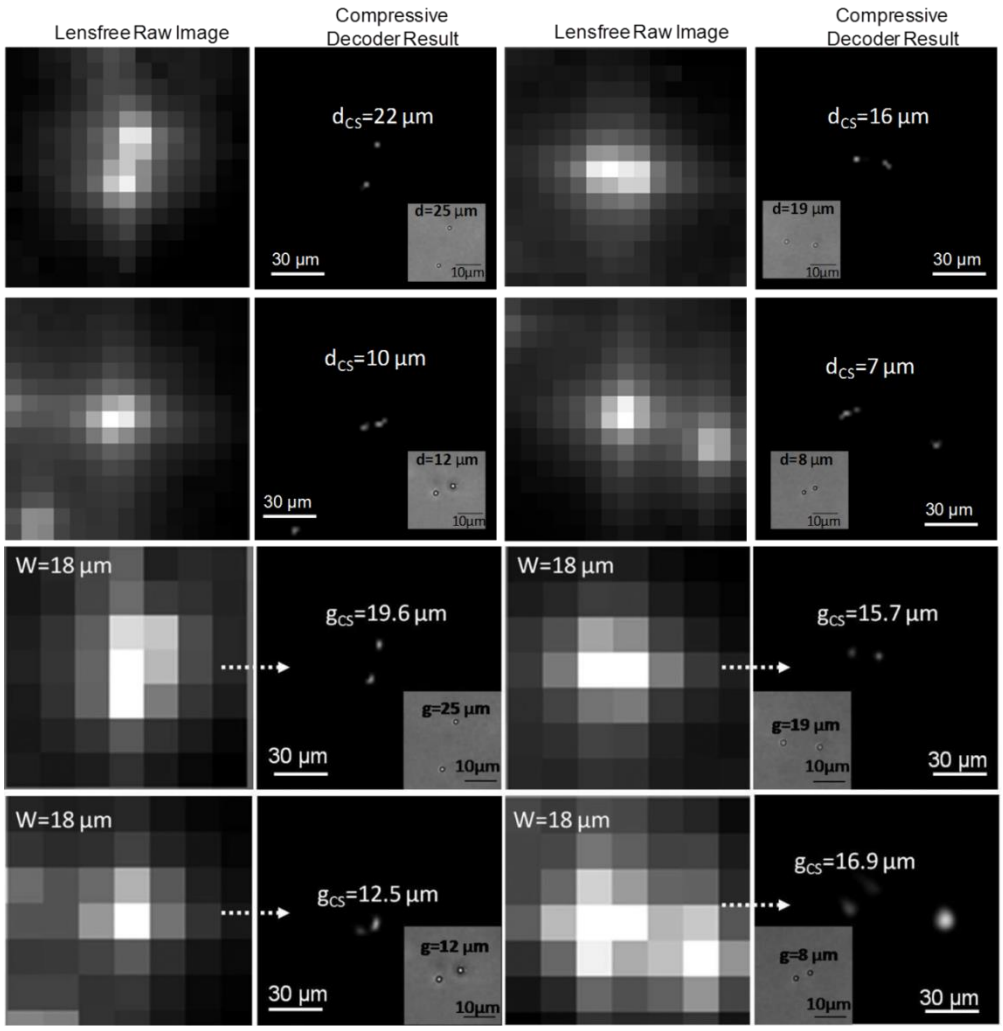

Figure 32: The raw lensfree images are decoded to resolve closely spaced particles from each other. The inset images (bottom right corner of each decoded image) illustrate regular transmission microscope images of the same particles from which the center-to-center distance (g) in each case is calculated for comparison purposes. The bottom row illustrates resolving 2µm particles that are separated by g ~12µm and 8µm. The pixel size in the raw lensfree fluorescent images is W = 9µm, whereas the pixel size of the decoded images is 2µm, i.e., N~20M. The point-spread function of the system has been estimated using 2 µm diameter fluorescent particles imaged at a low concentration. (2µm fluorescent particles) except with a pixel size of W = 18µm at the detector-array, such that 4 pixels of the CCD are now binned together. Similar to Figure 29, the raw lensfree images are decoded to resolve closely spaced fluorescent particles from each other. The pixel size of the decoded images is still 2µm, same as in Figure 29, which this time implies N = 81M. Because of a significant reduction in M when compared to Figure 29, the performance of the compressive decoding is relatively degraded, which is especially visible for reconstruction of g = 8µm case (bottom right corner). Regardless, even with N = 81M, decoding of sub-pixel objects as shown in e.g., g = 12 µm case is achieved.

It should also be noted that the fibers are dense and aligned regular enough for these fluorescent images to assume a shift-invariant PSF over each object plane, although they distorted the holographic images. Moreover, the presented lensfree approach is also able to reconstruct the distribution of fluorescent micro-objects located at multiple micro-channels that are stacked vertically as demonstrated in Figure 31. This increased the throughput of FLUOCHIP multiple folds by enabling to decode the 2D lensfree fluorescent image at the detector-array into a 3D distribution through compressive sampling.

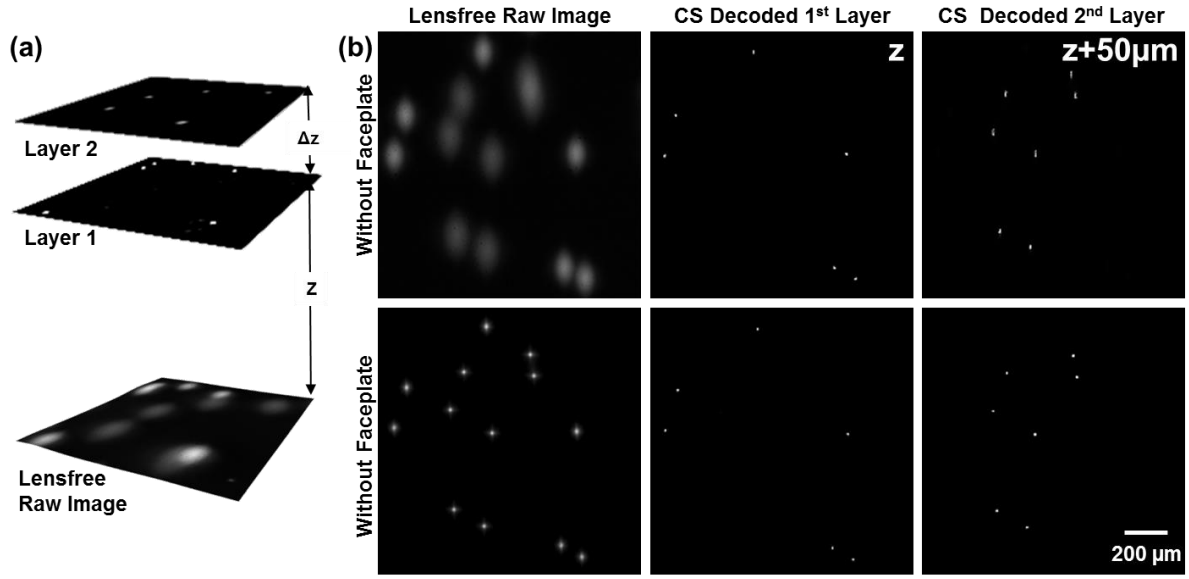

Figure 33: (a) Lensfree fluorescent imaging of 2 layers that are vertically separated by ~50μm is illustrated. (b1) shows a digitally cropped region of the large FOV that are imaged without the use of a faceplate. The compressive decoding results of this raw lensfree image for each vertical channel are illustrated in (b2-b3). The same region is also imaged using the faceplate as shown in (c1). The compressive decoding results of this lensfree image for each vertical channel are also illustrated in (c2-c3).

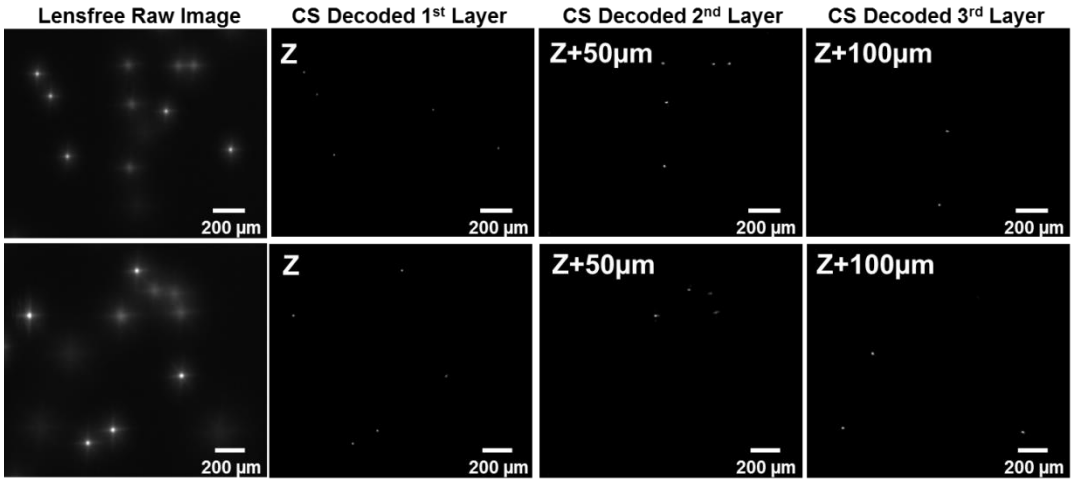

Figure 34: Same as in Figure 31, except for 3 fluorescent layers that are vertically separated by ~100 µm from each other. Two different regions are imaged using a faceplate, and the raw lensfree images are then decoded to reveal the distribution of the fluorescent particles at each layer. In the raw lensfree images, the fluorescent signatures from the 3rd layer are rather faint and need careful examination to see them with the bare eye, whereas the decoder output for the 3rd layer faithfully resolves their location. Such a computational strength would be quite significant to further increase the throughput in e.g., imaging cytometry experiments.

A descent spatial resolution of 10 µm for such a high-throughput device is already quite useful; however, some biological applications simply require seeing smaller objects or finer details. As a step towards satisfying this need, the system is modified by replacing the regular faceplate with a tapered faceplate such that the density of the fiber-optic waveguides on the top facet is ~5 fold larger than the bottom one (Figure 33).[14]

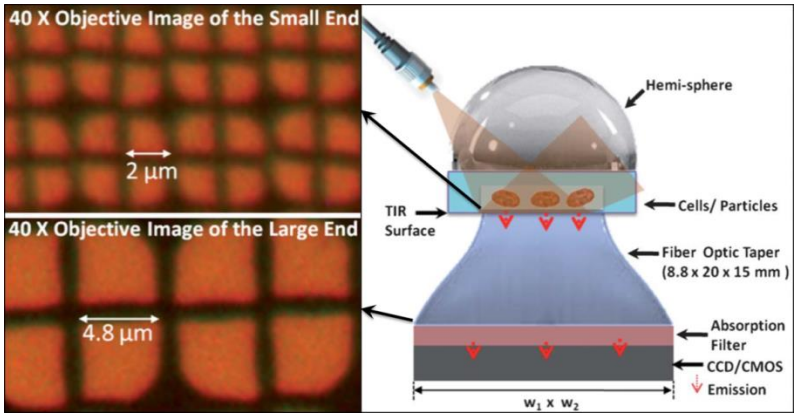

Figure 35: The schematic diagram of the lensfree fluorescent on-chip imaging platform is illustrated. (Right) Microscopic images of the top and bottom facets of the fiber-optic taper are shown. (Left) w1 = 25 mm and w2 =35 mm are used in this work.

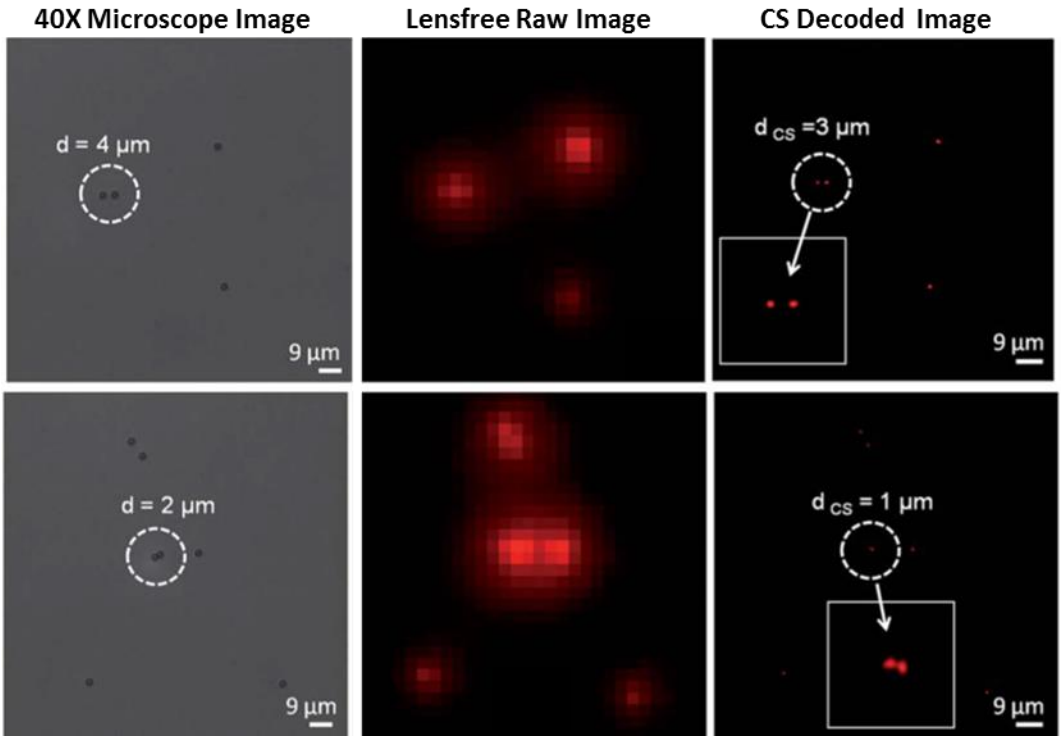

Figure 36: Resolution of the lensfree fluorescent on-chip microscope with taper is quantified using 2 µm diameter particles. The pixelated raw lensfree fluorescent images are decoded using a CS algorithm to resolve the overlapping lensfree fluorescent emission patterns arising from the particles. For comparison purposes conventional bright-field microscope images of the same 2 µm diameter particles are also shown on the left column. Note that because the samples were sequentially imaged using the microscope after their lensfree images were acquired, their relative orientations might be slightly rotated/ shifted between the two imaging modalities. The lensfree images are pseudo-colored in red.

As shown in Figure 34, the spatial resolution of this system is improved to ~2 µm by taking advantage of the 2.4X magnification factor of the tapered faceplate. Also labeled Giardia muris cysts are imaged as illustrated in Figure 35. These results show the potential of FLUOCHIP for rapid screening of water-borne parasites in field settings with its large FOV within a compact on-chip platform.

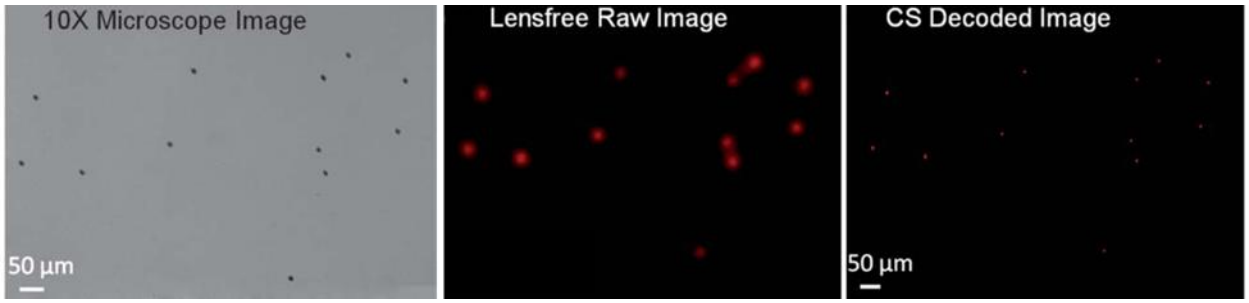

Figure 37: Lensfree fluorescent imaging results for Giardia muris cysts are shown. A conventional microscope image of the same FOV is also illustrated on left. Note that because the samples were sequentially imaged using the microscope after their lensfree images were acquired, their relative orientations might be slightly rotated/shifted between the two imaging modalities. The lensfree images are pseudo-colored in red.

4.4 Microscopy with On-chip Nano-Apertures (MONA)

To further improve the resolution to deeply subpixel levels, there is a need to break the coherency between the sparsifying and measurement bases. For this end, the shift-invariant on-chip imaging platform FLUOCHIP is turned into a position-dependent system by introducing a nano-structured metallic thin-film to modulate the PSF at each point on the chip. This technique is referred as **M**icroscopy with **O**n-chip **N**ano-**A**pertures (**MONA**). The basic working principle of MONA is illustrated in Figure 36. The light emitted from incoherent objects of interest e.g. fluorescent labeled cells which are directly positioned onto a nanostructured thin-metallic film is first modulated by the nanostructures. After diffracting over a short distance, it is sampled by a detector-array without the use of any lenses. The detected far-field diffraction pattern is then rapidly reconstructed by using an algorithm based on compressive decoding.

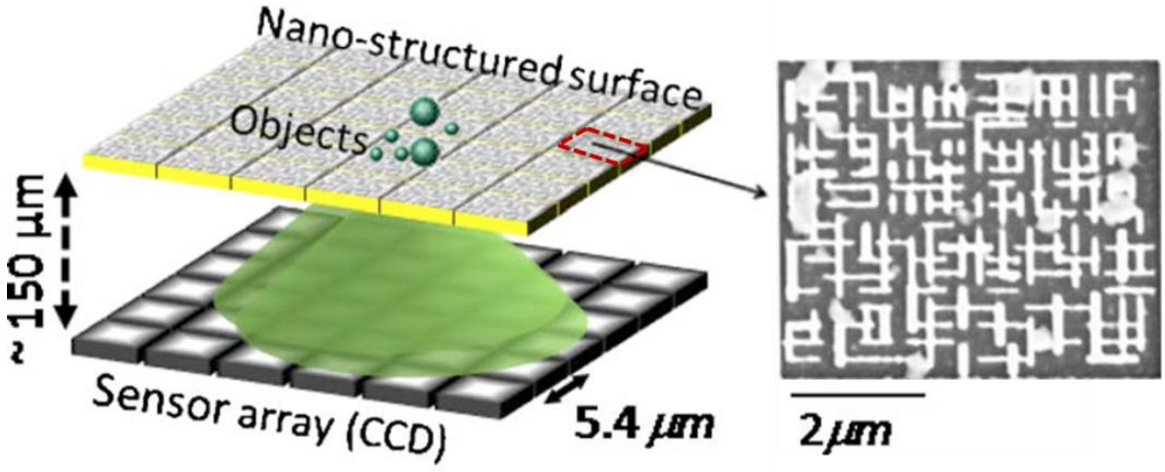

Figure 38: Schematic of lensfree on-chip imaging using a nanostructured surface is illustrated. SEM image of a structured chip is shown on the right.

This decoding process requires calibration of the nano-structured surface (Figure 36) serving as the object plane to form its specific measurement basis. It should be noted that the calibration step needs to be done only once for each chip by recording the unique diffraction patterns resulting from a tightly focused spot as it moves over the surface with a deeply sub-pixel step size. These calibrations are also used to iteratively optimize the nano-patterns for breaking the correlation between the diffraction patterns of closely spaced points (Figure 37, b-c).

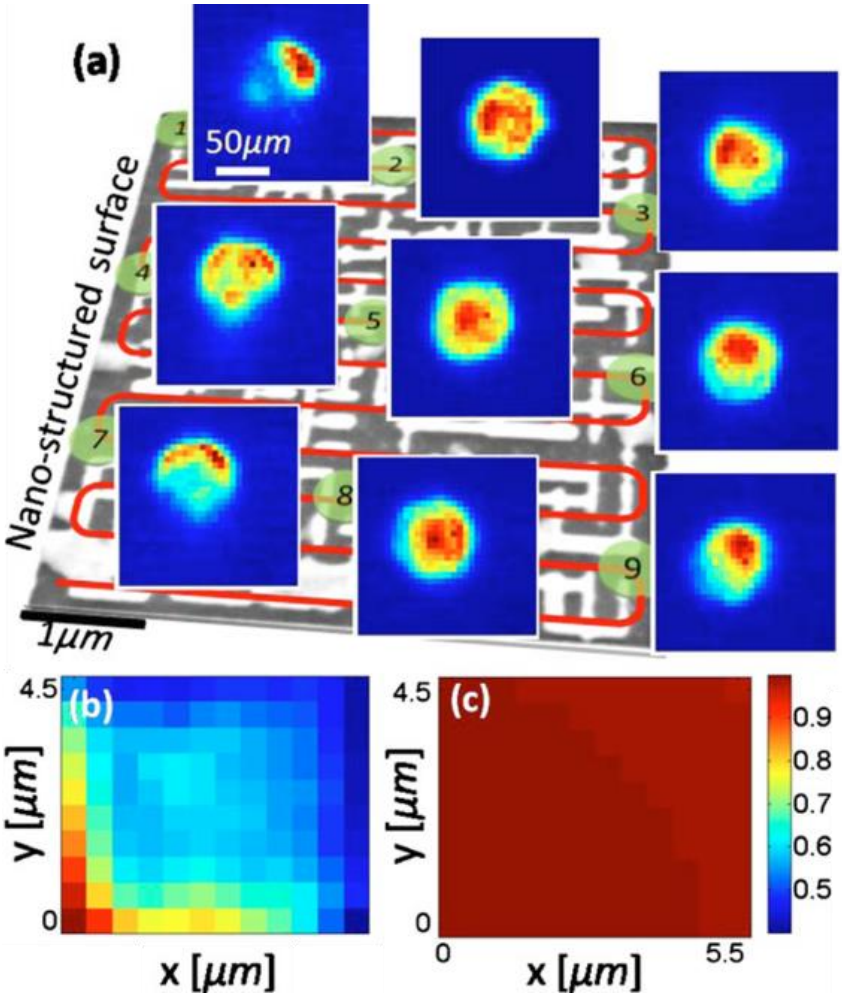

Figure 39: (a) Calibration process of a nanostructured transmission surface is outlined. Several far-field calibration images of the patterned chip shown in previous figure are also provided. (b) Cross-correlation coefficients of the first calibration frame against all the other calibration images of the same chip are illustrated. (c) Same as part (b), except this time it is measured for a bare glass substrate without the nanostructures. Significantly higher cross-correlation observed in (c) for closely spaced points, is the reason for limited spatial resolution of conventional lensfree incoherent imaging without the nanostructures. Nanostructured surfaces break this correlation as shown in (b) to achieve a significantly better resolution.

As a proof of concept experiment [15], nano-apertures are punched over a ~5 μm^2 area on a gold coated glass surface and calibrated it with 0.5 μm step size. Then the raw lensfree diffraction images are recorded from two very close spots by using a CCD with 5.4 μm pixel size. Figure 38 shows the raw lensfree images and the sub-pixel decoding results together with microscope comparisons.

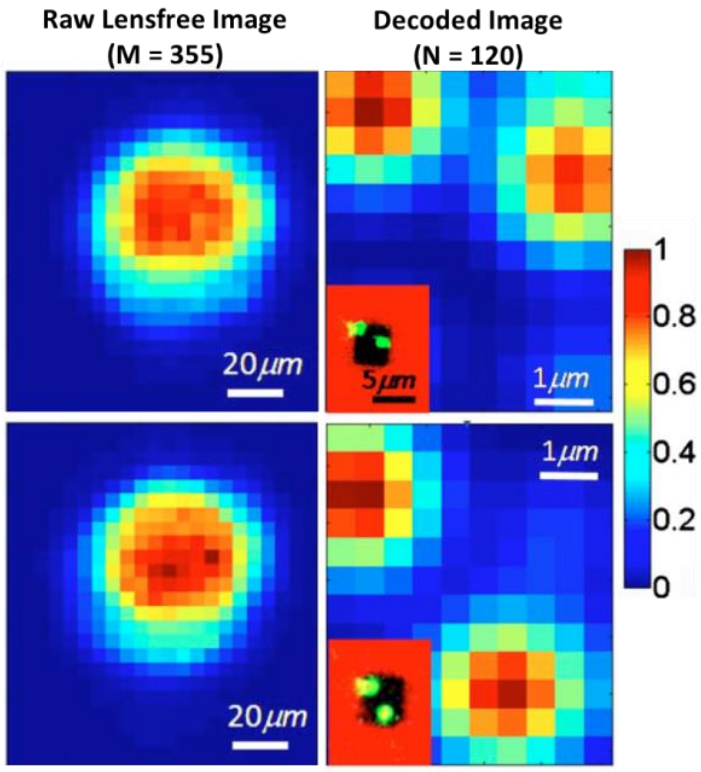

Figure 40: Experimental proof-of-concept of lensfree on-chip imaging using the nano-structured surface is demonstrated. Left column shows the lensfree diffraction images of the objects sampled at the CCD for two different incoherent objects. Each diffraction image contains M =355 pixels. Right column shows the compressive decoding results of these raw diffraction images to resolve sub-pixel objects on the chip. For comparison, the inset images in the bottom row show regular reflection microscope images of the objects, which very well agree with the reconstruction results. Note that the red colored regions of the inset images refer to the gold coated area with no transmission, and therefore the reconstructions only focus to the dark regions of the chip (at the center of the inset images) that are nano-patterned.

To better appreciate the compressive nature of the method, the performance of the decoding algorithm is reported in Figure 39, when the used number of pixel is far less than the recovered number of points. All these results verify that MONA could especially be useful to create very high-resolution lensfree fluorescent microscopes on a compact chip.

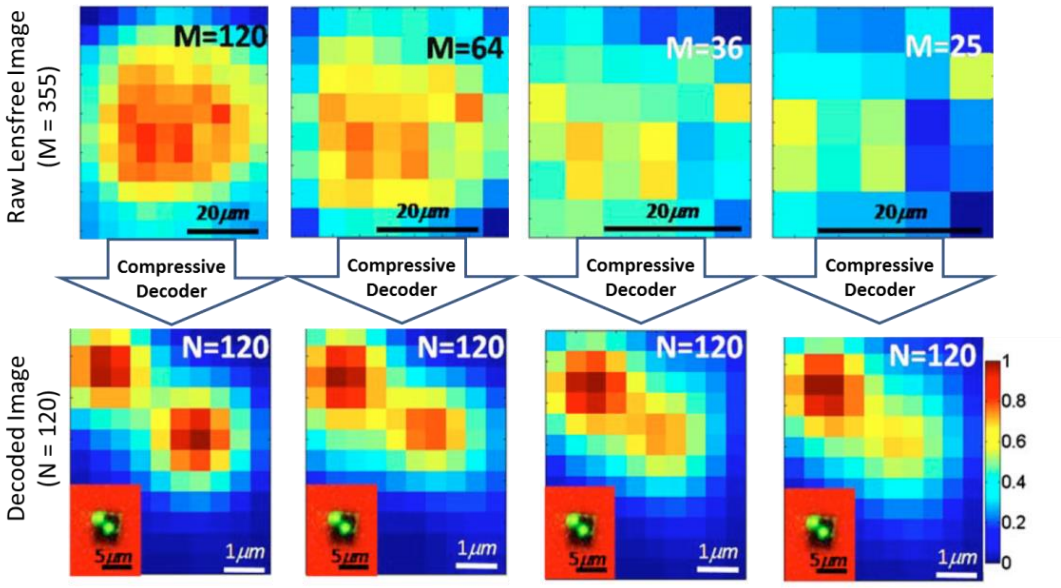

Figure 41: Performance of the decoder for different M values. This figure indicates that compressive decoding of a sparse object can be achieved from its diffraction pattern at the far-field even for an under-sampled imaging condition where N>M.

4.5 Color-MONA

As the next step, on-chip incoherent color imaging with MONA is demonstrated. To add this important property of full color imaging to the system, the calibration basis is extended by using red, green and blue focused spots. These point sources at each color (RGB) scans the surface of the structured substrate, while the sensor-array is recording the resulting lensfree diffraction patterns corresponding to each spot on the structured chip. Also an RGB sensor is preferred to use with raw output to increase the modulation as a function of color and to provide color comparison for better appreciation of the spatial and color resolving power of this system.

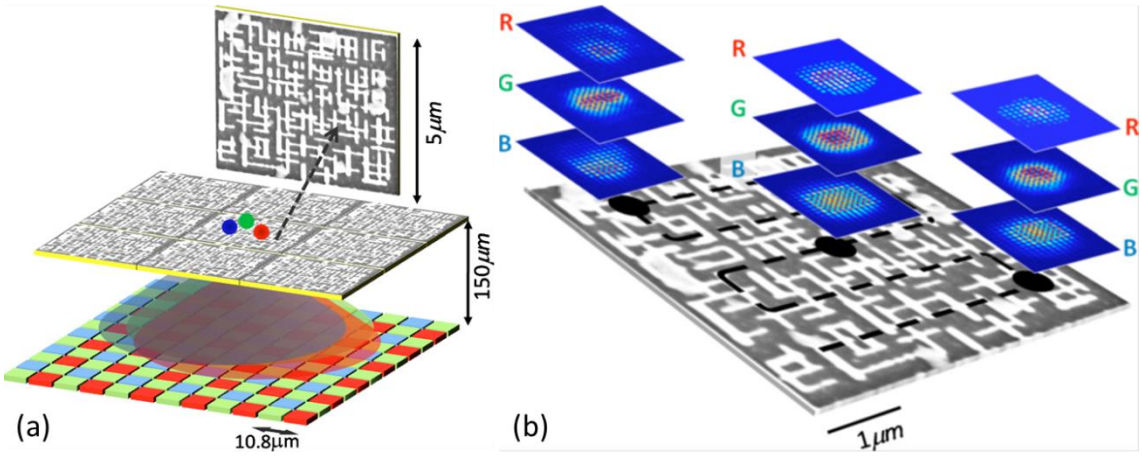

Figure 42: Color-MONA

Figure 40 shows the raw images and the compressive decoding result of three RGB spots which are closely packed into a single pixel area. The agreement between the decoded image and the 40X microscope comparison suggest that MONA has a great potential to perform compact, on-chip color imaging with deeply sub-pixel resolution. This chip can be tiled up to cover all sensor active area and perform real fluorescent imaging experiments.

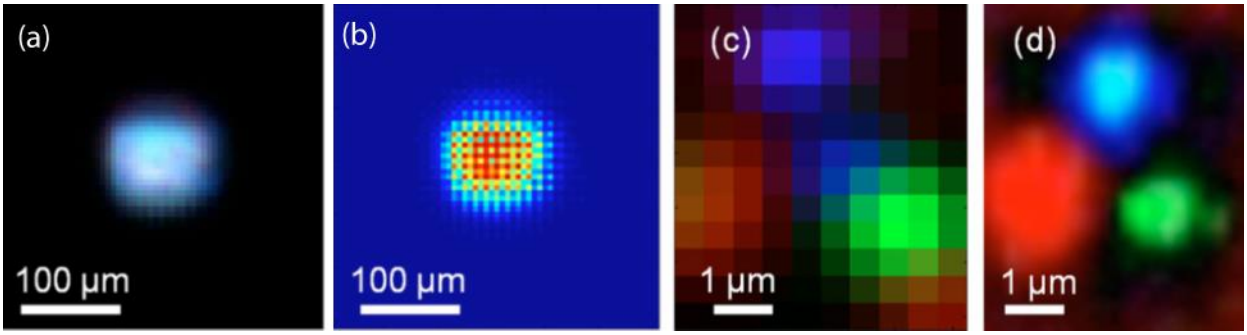

Figure 43: (a) Demosaiced lensfree diffraction image of a subpixel multicolor object is illustrated. This object is composed of RGB spots that are separated from each other by 1–2 μm. As expected, the far-field diffraction pattern of closely packed RGB spots creates a white-looking enlarged pattern. The same subpixel object is also imaged using a conventional reflection microscope 40X objective lens, numerical aperture = 0.6 as illustrated in (d) for comparison purposes. (b) presents the same raw lensfree image as in (a) before a demosaicing algorithm is applied. (c) successfully demonstrates the compressive decoding results based on processing of the raw lensfree diffraction pattern shown in (b)Notice that the scale-bars in (a) and (b) are 100 fold larger than the ones in (c) and (d).

4.6 Discussion

In this subsection, first some possible ways to further improve the performance of the FLUOCHIP is discussed and then some proof of concept work is reported towards infrared implementation of MONA.

The regulation parameter (β) is an effective parameter in FLUOCHIP reconstructions, since it balances the fidelity and regularization terms of the optimization problem as discussed earlier in Chapter 4. Setting very large β values($\beta > \beta_{max}$) leads to all zero recoveries, whereas using extremely small β values simply results regular least square minimizations without any sparsity constraint applied.

$$\beta_{max} = \|2A^T y\|_\infty \qquad (18)$$

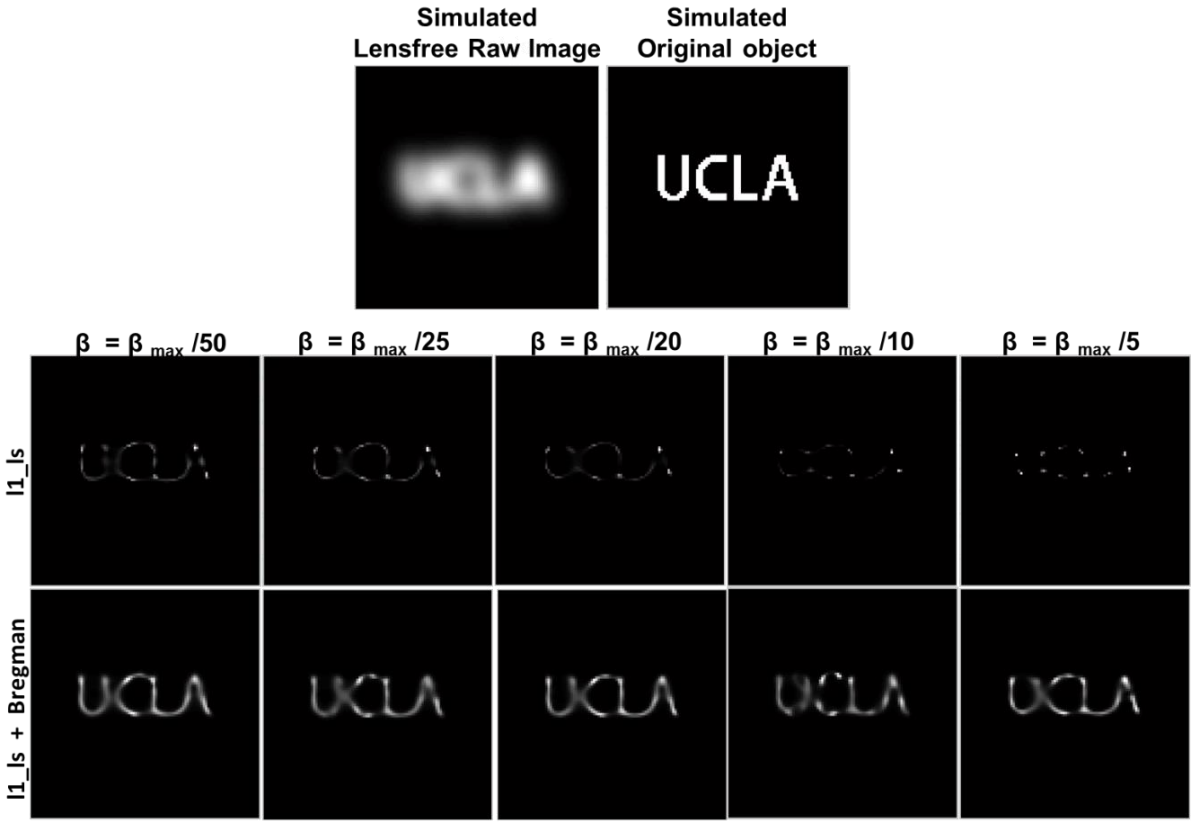

Figure 44: Effect of regularization parameter on the l1 regularized least square recoveries with and without Bregman step

This β-dependence of the l1_ls recoveries (Figure 44, middle row) can be relaxed by adding a Bregman step [49], [50].

$$y_{k+1} = y + y_k - Ax_k \quad (19)$$

$$x_{k+1} = \arg\min(\beta \|x_k\|_1 + \|Ax - y_{k+1}\|_2^2) \quad (20)$$

As demonstrated on simulated recoveries in bottom row of Figure 44, the l1 regularized least square minimizations modified with a Bregman step provided the flexibility to work over a wide range of β. Although for most of the FLUOCHIP recoveries reported in this dissertation, setting regularization parameters around ~β_{max}/10 gave satisfying results, this approach can be further studied and implemented in future for FLUOCHIP implementations, where fine tuning of regularization parameter may be needed.

Another future direction in FLUOCHIP implementation is to employ structured illumination combined with compressive decoding to develop a higher resolution, perhaps an adaptive system for better addressing the needs of rare-event detection in highly scattering mediums e.g. circulating tumor cell detection within whole blood. Earlier work of Arpali et al. [51] suggests that replacing the uniform illumination with multiple known structured patterns (Gaussian spots) created with a spatial light modulator reduces the background caused by leakage of the scattered light and increases the SNR. This approach can implement it within an adaptive flow to improve our spatial resolution without being compromised by highly scattering mediums. Usage of compressive sensing with random patterns can enable us to achieve this goal faster by minimizing the number of illumination patterns needed.

One future work for high resolution incoherent imaging by using nanostructured surfaces (MONA platform) can be the demonstration of the performance with a MONA chip scaled to cover whole sensor surface. Besides, the infrared (IR) implementation of MONA can be very valuable because it can significantly reduce the high cost of high resolution, wide-field IR

detectors. Moreover, it is easier to fabricate and optimize a MONA chip for IR than for the visible range. Towards this end, proof-of-concept, IR MONA experiments are performed.

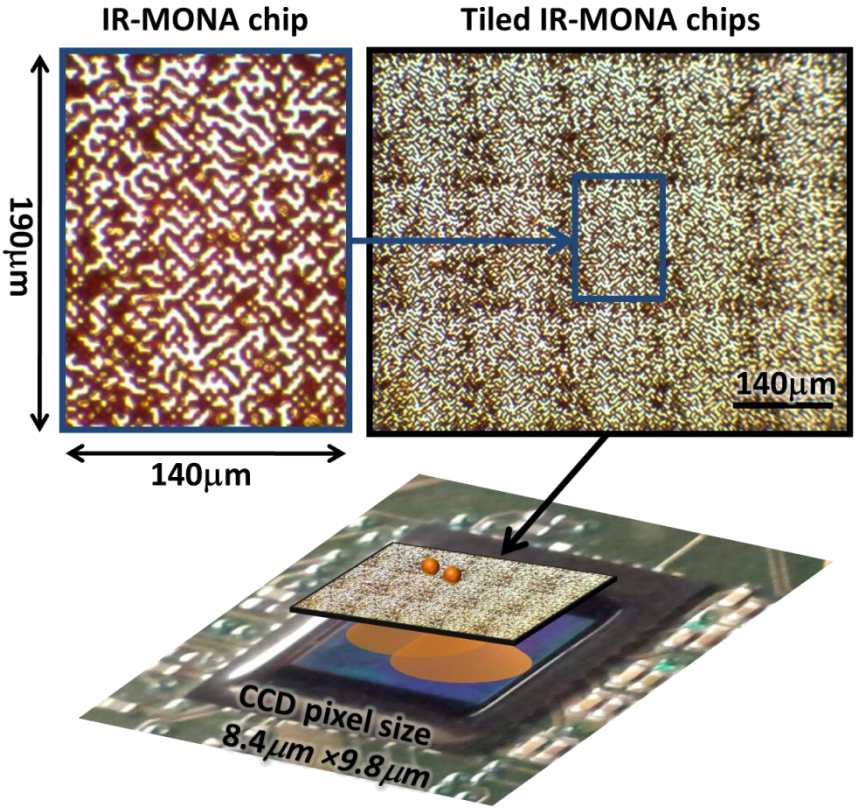

Figure 45: The microscope image of a fabricated IR-MONA chip, the tiled version and illustration of IR-MONA platform

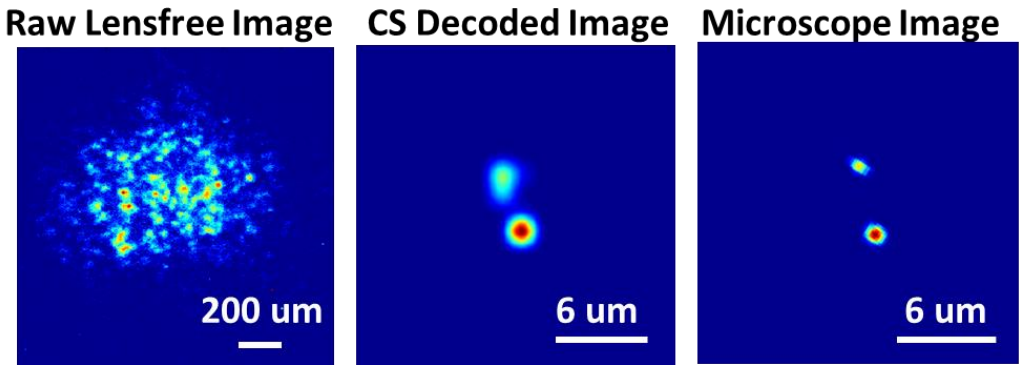

Figure 46: The raw infrared lensfree intensity detected after the structured surface (left), the compressive sensing based recovery result(middle) and the microscope comparison(right)

The IR-MONA chip is prepared as done in visible range, except that the apertures are wider. A pulsed laser of 1550 nm wavelength is used to calibrate the chip. Then the chip is illuminated with two spots of the same wavelength separated by ~5μm, which served as an object, which requires deeply subpixel resolution to be recovered. The raw IR-MONA image is successfully reconstructed by using as reported in Figure 46. This result suggests that IR-MONA is a promising high-resolution infrared imaging platform, which can be studied more comprehensively and used for practical applications in future.

Chapter 5 Conclusion

Lensfree computational imaging and sensing techniques provide opportunities to replace bulky and expensive designs of conventional microscopes with much simpler, compact and cost-effective on-chip imaging architectures, which can achieve decent spatial resolution and sensitivity over a significantly large imaging area. In this dissertation, some lensfree computational microscopy platforms and their biomedical applications are summarized after providing general background on the computational methods employed in these tools to compensate the shortcomings of lensfree geometries: Iterative phase retrieval methods tailored for lensfree geometries are used to focus the diffracted lensfree signatures, retrieve the complex field from intensity measurements and simultaneously eliminate the twin image noise of the inline holography. For objects with very high spatial frequencies, where the pixel size of the detector array limit the resolution, I employed pixel super resolution methods for lensfree imaging based on source shifting to eliminate undersampling and aliasing artifacts. Also, I used specially tailored Compressive Sensing based optimizations to demultiplex superimposed spectral content of holographic and fluorescent signatures and for high resolution incoherent imaging over extreme field of views.

These platforms and their applications are presented under two main category based on the coherence level of the illumination source. Imaging and sensing platforms working based on partially coherent lensfree holography are reported in Chapter 3 in an order that the portability of the system gradually increases: First some initial bench top implementations are reported for high throughput blood analysis and small animal observations in color. Then a portable, light-weight, and cost-effective standalone unit and a cellphone attachment are demonstrated for telemedicine applications like drinking water screenings or blood analysis on low resource field-settings. After introducing the polychromatic phase retrieval as a computational solution towards addressing the lack of temporal coherence and artifacts due to the broadband spectral nature of LEDs, I demonstrated a field-portable lensfree, super-resolution, holographic microscope

working with sunlight illuminations. This chapter is concluded with a proof of concept on-chip lensfree sensing implementation for detection of bulk refractive index change in liquids. In Chapter 4, I listed incoherent, specifically fluorescent, imaging platforms, with microfluidics friendly on-chip design and extreme filed of views. I presented these platforms in an order with increasing complexity and improved spatial resolution. First, I introduced the monochromatic and multicolor FLUOCHIP and how the use of fiber optic faceplates and tapers improved the signal to noise ratio and the resolution of the system. Then MONA is reported showing how nanostructured metallic surfaces can be used to create position dependent point spread functions and further improve the resolution of the incoherent on-chip imaging system to deep subpixel level, even for multicolor.

I strongly believe that these computational lensfree microscopy platforms, a deep and broad understanding about their operation ranges, advantages and limitations will serve greatly towards developing more unconventional imaging and sensing approaches. These devices will more effectively address the specific needs of several biomedical applications as the optoelectronic components and computational methods quickly advance and fill a gap in imaging area with their unique throughput and portability advantages.

References

[1] S. O. Isikman, I. Sencan, O. Mudanyali, W. Bishara, C. Oztoprak, and A. Ozcan, “Color and monochrome lensless on-chip imaging of Caenorhabditis elegans over a wide field-of-view,” *Lab Chip*, vol. 10, no. 9, pp. 1109–1112, Mar. 2010.

[2] O. Mudanyali, D. Tseng, C. Oh, S. O. Isikman, I. Sencan, W. Bishara, C. Oztoprak, S. Seo, B. Khademhosseini, and A. Ozcan, “Compact, light-weight and cost-effective microscope based on lensless incoherent holography for telemedicine applications,” *Lab Chip*, vol. 10, no. 11, pp. 1417–1428, Apr. 2010.

[3] S. Seo, S. O. Isikman, I. Sencan, O. Mudanyali, T.-W. Su, W. Bishara, A. Erlinger, and A. Ozcan, “High-Throughput Lens-Free Blood Analysis on a Chip,” *Anal Chem*, vol. 82, no. 11, pp. 4621–4627, 2010.

[4] S. O. ISIKMAN, W. Bishara, O. Mudanyali, I Sencan, T. W. Su, D. Tseng, O. Yaglidere, U. Sikora, and A. Ozcan, “Lensfree On-Chip Microscopy and Tomography for Bio-Medical Applications,” *IEEE J. Sel. Top. Quantum Electron.*, vol. PP, no. 99, pp. 1–1.

[5] A. F. Coskun, I. Sencan, T.-W. Su, and A. Ozcan, “Lensless wide-field fluorescent imaging on a chip using compressive decoding of sparse objects,” *Opt. Express*, vol. 18, no. 10, pp. 10510–10523, May 2010.

[6] A. Greenbaum, W. Luo, T.-W. Su, Z. Göröcs, L. Xue, S. O. Isikman, A. F. Coskun, O. Mudanyali, and A. Ozcan, “Imaging without lenses: achievements and remaining challenges of wide-field on-chip microscopy,” *Nat. Methods*, vol. 9, no. 9, pp. 889–895, Sep. 2012.

[7] E. J. Candes and M. B. Wakin, “An Introduction To Compressive Sampling,” *Signal Process. Mag. IEEE*, vol. 25, no. 2, pp. 21–30, 2008.

[8] R. G. Baraniuk, “Compressive Sensing [Lecture Notes],” *Signal Process. Mag. IEEE*, vol. 24, no. 4, pp. 118–121, 2007.

[9] E. Betzig, G. H. Patterson, R. Sougrat, O. W. Lindwasser, S. Olenych, J. S. Bonifacino, M. W. Davidson, J. Lippincott-Schwartz, and H. F. Hess, “Imaging Intracellular Fluorescent Proteins at Nanometer Resolution,” *Science*, vol. 313, no. 5793, pp. 1642–1645, Sep. 2006.

[10] M. G. L. Gustafsson, “Nonlinear structured-illumination microscopy: Wide-field fluorescence imaging with theoretically unlimited resolution,” *Proc. Natl. Acad. Sci.*, vol. 102, no. 37, pp. 13081–13086, Sep. 2005.

[11] M. J. Rust, M. Bates, and X. Zhuang, “Sub-diffraction-limit imaging by stochastic optical reconstruction microscopy (STORM),” *Nat. Methods*, vol. 3, no. 10, pp. 793–796, Aug. 2006.

[12] S. T. Hess, T. P. K. Girirajan, and M. D. Mason, “Ultra-High Resolution Imaging by Fluorescence Photoactivation Localization Microscopy,” *Biophys. J.*, vol. 91, no. 11, pp. 4258–4272, Dec. 2006.

[13] D. Tseng, O. Mudanyali, C. Oztoprak, S. O. Isikman, I. Sencan, O. Yaglidere, and A. Ozcan, “Lensfree microscopy on a cellphone,” *Lab Chip*, vol. 10, no. 14, pp. 1787–1792, May 2010.

[14] A. F. Coskun, I. Sencan, T.-W. Su, and A. Ozcan, “Wide-field lensless fluorescent microscopy using a tapered fiber-optic faceplate on a chip,” *Analyst*, vol. 136, no. 17, pp. 3512–3518, Jan. 2011.

[15] B. Khademhosseinieh, I. Sencan, G. Biener, T.-W. Su, A. F. Coskun, D. Tseng, and A. Ozcan, “Lensfree on-chip imaging using nanostructured surfaces,” *Appl. Phys. Lett.*, vol. 96, p. 171106, 2010.

[16] B. Khademhosseinieh, G. Biener, I. Sencan, and A. Ozcan, “Lensfree color imaging on a nanostructured chip using compressive decoding,” *Appl. Phys. Lett.*, vol. 97, p. 211112, 2010.
[17] W. Bishara, T.-W. Su, A. F. Coskun, and A. Ozcan, “Lensfree on-chip microscopy over a wide field-of-view using pixel super-resolution,” *Opt. Express*, vol. 18, no. 11, pp. 11181–11191, May 2010.
[18] S. O. Isikman, W. Bishara, H. Zhu, and A. Ozcan, “Optofluidic Tomography on a Chip,” *Appl. Phys. Lett.*, vol. 98, no. 16, pp. 161109–161109–3, Apr. 2011.
[19] R. W. Gerchberg and W. O. Saxton, “A practical algorithm for the determination of phase from image and diffraction plane pictures,” *Optik*, vol. 35, no. 2, pp. 237–246, 1972.
[20] J. R. Fienup, “Phase retrieval algorithms: a comparison,” *Appl. Opt.*, vol. 21, no. 15, pp. 2758–2769, 1982.
[21] J. W. Goodman, *Introduction To Fourier Optics*. Roberts and Company Publishers, 2005.
[22] Moravec, “Compressive Phase Retrieval,” 2007. .
[23] G. Liu and P. D. Scott, “Phase retrieval and twin-image elimination for in-line Fresnel holograms,” *JOSA*, vol. 4, no. 1, pp. 159–165, 1987.
[24] J. Goodman, *Introduction to Fourier Optics*, 3rd Edition. Roberts and Company Publishers, 2004.
[25] S. W. Hell, “Toward fluorescence nanoscopy,” *Nat. Biotechnol.*, vol. 21, no. 11, pp. 1347–1355, Nov. 2003.
[26] R. C. Gonzalez and R. E. Woods, *Digital Image Processing*, 2nd ed. Prentice Hall, 2002.
[27] D. L. Donoho, “Compressed sensing,” *Inf. Theory IEEE Trans.*, vol. 52, no. 4, pp. 1289–1306, 2006.
[28] E. J. Candès, “The restricted isometry property and its implications for compressed sensing,” *Comptes Rendus Math.*, vol. 346, no. 9–10, pp. 589–592, May 2008.
[29] S.-J. Kim, K. Koh, M. Lustig, S. Boyd, and D. Gorinevsky, “An Interior-Point Method for Large-Scale L1-Regularized Least Squares,” *Sel. Top. Signal Process. IEEE J.*, vol. 1, no. 4, pp. 606–617, 2007.
[30] J. M. Bioucas-Dias and M. A. T. Figueiredo, “A New TwIST: Two-Step Iterative Shrinkage/Thresholding Algorithms for Image Restoration,” *Image Process. IEEE Trans.*, vol. 16, no. 12, pp. 2992–3004, 2007.
[31] D. J. Brady, K. Choi, D. L. Marks, R. Horisaki, and S. Lim, “Compressive Holography,” *Opt. Express*, vol. 17, no. 15, pp. 13040–13049, Jul. 2009.
[32] M. M. Marim, M. Atlan, E. D. Angelini, and J.-C. Olivo-Marin, “Compressed sensing for digital holographic microscopy,” in *Biomedical Imaging: From Nano to Macro, 2010 IEEE International Symposium on*, 2010, pp. 684–687.
[33] L. Denis, D. Lorenz, E. Thibaut, C. Fournier, and D. Trede, “Inline hologram reconstruction with sparsity constraints,” *Opt. Lett.*, vol. 34, no. 22, pp. 3475–3477, Nov. 2009.
[34] B. Khademhosseinieh, G. Biener, I. Sencan, T.-W. Su, A. F. Coskun, and A. Ozcan, “Lensfree sensing on a microfluidic chip using plasmonic nanoapertures,” *Appl. Phys. Lett.*, vol. 97, p. 221107, 2010.
[35] D. C. Ghiglia and M. D. Pritt, *Two-dimensional phase unwrapping: theory, algorithms, and software*. Wiley, 1998.
[36] W. Bishara, U. Sikora, O. Mudanyali, T.-W. Su, O. Yaglidere, S. Luckhart, and A. Ozcan, “Holographic pixel super-resolution in portable lensless on-chip microscopy using a fiber-optic array,” *Lab. Chip*, vol. 11, no. 7, p. 1276, 2011.
[37] S. O. Isikman, W. Bishara, S. Mavandadi, F. W. Yu, S. Feng, R. Lau, and A. Ozcan, “Lens-free optical tomographic microscope with a large imaging volume on a chip,” *Proc. Natl. Acad. Sci.*, Apr. 2011.
[38] R. Kimmel, “Demosaicing: image reconstruction from color CCD samples,” *IEEE Trans. Image Process.*, vol. 8, no. 9, pp. 1221–1228, Sep. 1999.

[39] Y. Liu, J. C. Andrews, J. Wang, F. Meirer, P. Zhu, Z. Wu, and P. Pianetta, “Phase retrieval using polychromatic illumination for transmission X-ray microscopy,” *Opt. Express*, vol. 19, no. 2, pp. 540–545, Jan. 2011.
[40] “The Influence of the Condenser on Microscopic Resolution.” .
[41] M. Locatelli, E. Pugliese, M. Paturzo, V. Bianco, A. Finizio, A. Pelagotti, P. Poggi, L. Miccio, R. Meucci, and P. Ferraro, “Imaging live humans through smoke and flames using far-infrared digital holography,” *Opt. Express*, vol. 21, no. 5, pp. 5379–5390, Mar. 2013.
[42] N. George, K. Khare, and W. Chi, “Infrared holography using a microbolometer array,” *Appl. Opt.*, vol. 47, no. 4, pp. A7–A12, Feb. 2008.
[43] L. Repetto, R. Chittofrati, E. Piano, and C. Pontiggia, “Infrared lensless holographic microscope with a vidicon camera for inspection of metallic evaporations on silicon wafers,” *Opt. Commun.*, vol. 251, no. 1–3, pp. 44–50, Jul. 2005.
[44] M. Paturzo, A. Finizio, P. Memmolo, R. Puglisi, D. Balduzzi, A. Galli, and P. Ferraro, “Microscopy imaging and quantitative phase contrast mapping in turbid microfluidic channels by digital holography,” *Lab. Chip*, vol. 12, no. 17, p. 3073, 2012.
[45] A. F. Coskun, T. Su, I. Sencan, and A. Ozcan, “Lensfree Fluorescent On-Chip ImagingUsing Compressive Sampling,” *Opt. Photonics News*, vol. 21, no. 12, p. 27, Dec. 2010.
[46] A. F. Coskun, I. Sencan, T.-W. Su, and A. Ozcan, “Lensfree Fluorescent On-Chip Imaging of Transgenic Caenorhabditis elegans Over an Ultra-Wide Field-of-View,” *PLoS ONE*, vol. 6, no. 1, p. e15955, Jan. 2011.
[47] A. F. Coskun, T.-W. Su, I. Sencan, and A. Ozcan, “Lensless Fluorescent Microscopy on a Chip,” *J. Vis. Exp.*, no. 54, Aug. 2011.
[48] Seung-Jean Kim, K. Koh, M. Lustig, S. Boyd, and D. Gorinevsky, “An Interior-Point Method for Large-Scale l1-Regularized Least Squares,” *Sel. Top. Signal Process. IEEE J.*, vol. 1, no. 4, pp. 606–617, 2007.
[49] L. M. Bregman, “The relaxation method of finding the common point of convex sets and its application to the solution of problems in convex programming,” *USSR Comput. Math. Math. Phys.*, vol. 7, no. 3, pp. 200–217, 1967.
[50] J.-F. Cai, S. Osher, and Z. Shen, “Linearized Bregman iterations for compressed sensing,” *Math. Comput.*, vol. 78, no. 267, pp. 1515–1536, 2009.
[51] S. A. Arpali, C. Arpali, A. F. Coskun, H.-H. Chiang, and A. Ozcan, “High-throughput screening of large volumes of whole blood using structured illumination and fluorescent on-chip imaging,” *Lab. Chip*, vol. 12, no. 23, pp. 4968–4971, Oct. 2012.